Tidally induced diapycnal mixing in the Kuril Straits and its role in water transformation and transport: A three-dimensional nonhydrostatic model experiment

Tomohiro Nakamura[1] and Toshiyuki Awaji[2]

Department of Geophysics, Graduate School of Science, Kyoto University, Kyoto, Japan

Received 11 March 2003; revised 12 November 2003; accepted 20 January 2004; published 1 July 2004.

[1] Baroclinic processes generated by the K_1 tidal flow around the Kuril Straits and their role in the linkage between the Okhotsk Sea and the North Pacific are investigated using a three-dimensional nonhydrostatic model. Large-amplitude unsteady lee waves are generated around sill tops all along the Kuril Island Chain and induce significant density inversions from the sea surface down to the $\sim$27.6 σ_θ density layer. Along with this wave breaking, a large flow of energy takes place from the swift tidal flow regions to greater depths as a result of the clockwise propagation of both the topographically trapped waves around the islands and the remaining unsteady lee waves. Such wave generation and energy exchange eventually cause intense diapycnal mixing over the shallow topographic features and near the bottom, leading to a maximum diapycnal diffusivity of over 10^3 cm^2 s^{-1}. Even in the deep Bussol' Strait, which is thought to be the main exit of the Okhotsk Sea water, considerable mixing (corresponding to diapycnal diffusivity values of between $10 \sim 50$ cm^2 s^{-1}) occurs. Vigorous mixing in the shallow regions produces low potential vorticity (PV) water in the upper layer and high PV water below. Accordingly, PV fronts are formed along the island chain and sustain instabilities that in turn release baroclinic eddies with low core PV values. These features are indicated in recent satellite imagery and in situ observations, suggesting that the tide is the controlling factor in the formation of fronts observed in the Kuril Straits. Tidally induced mean transport across the straits is estimated to reach $\sim$26 Sv (1 Sv = 10^6 m^3 s^{-1}), which is much larger than in the barotropic case. However, most of the exchanged water tends to circulate around the islands due to the effect of bottom topography, whereas eddies pinched off from the tidal fronts carry the exchanged water offshore. The amount of eddy-driven offshore transport away from the islands reaches 14 Sv, with roughly half being directed to the North Pacific. This significant offshore transport spreads the effect of the diapycnal mixing taking place in the straits over wider areas of the North Pacific and the Okhotsk Sea. For example, the PV values generated in the eddies differ by 30–40% from the ambient water on average, whereas sea surface salinity within the eddies is 0.1 psu higher than the surroundings, corresponding to the density increase of 0.08 σ_θ. Thus the eddy transport provides significant PV and salinity fluxes to both the North Pacific and the Okhotsk Sea. Hence we infer that a combination of tidally driven processes taking place at the passages leads to the formation of eddies that play a central role in water transport and transformation and are an essential aspect of the physical interplay between the Okhotsk Sea and the North Pacific. *INDEX TERMS:* 4520 Oceanography: Physical: Eddies and mesoscale processes; 4544 Oceanography: Physical: Internal and inertial waves; 4219 Oceanography: General: Continental shelf processes; 4255 Oceanography: General: Numerical modeling; *KEYWORDS:* Kuril Straits, internal wave, diapycnal mixing, tidal front, eddy-induced transport, tidal rectification

Citation: Nakamura, T., and T. Awaji (2004), Tidally induced diapycnal mixing in the Kuril Straits and its role in water transformation and transport: A three-dimensional nonhydrostatic model experiment, *J. Geophys. Res.*, *109*, C09S07, doi:10.1029/2003JC001850.

1. Introduction

[2] The Okhotsk Sea (Figure 1) is separated from the northwestern Pacific Ocean by the Kuril Islands and the sills in the straits, almost all of which are shallower than 600 m except for the Bussol' ($\sim$2200 m) and the Kruzenshterna

[1] Now at Integrated Modeling Program, Frontier Research System for Global Change, Yokohama, Japan.

[2] Also at Integrated Modeling Program, Frontier Research System for Global Change, Yokohama, Japan.

0148-0227/04/2003JC001850$09.00

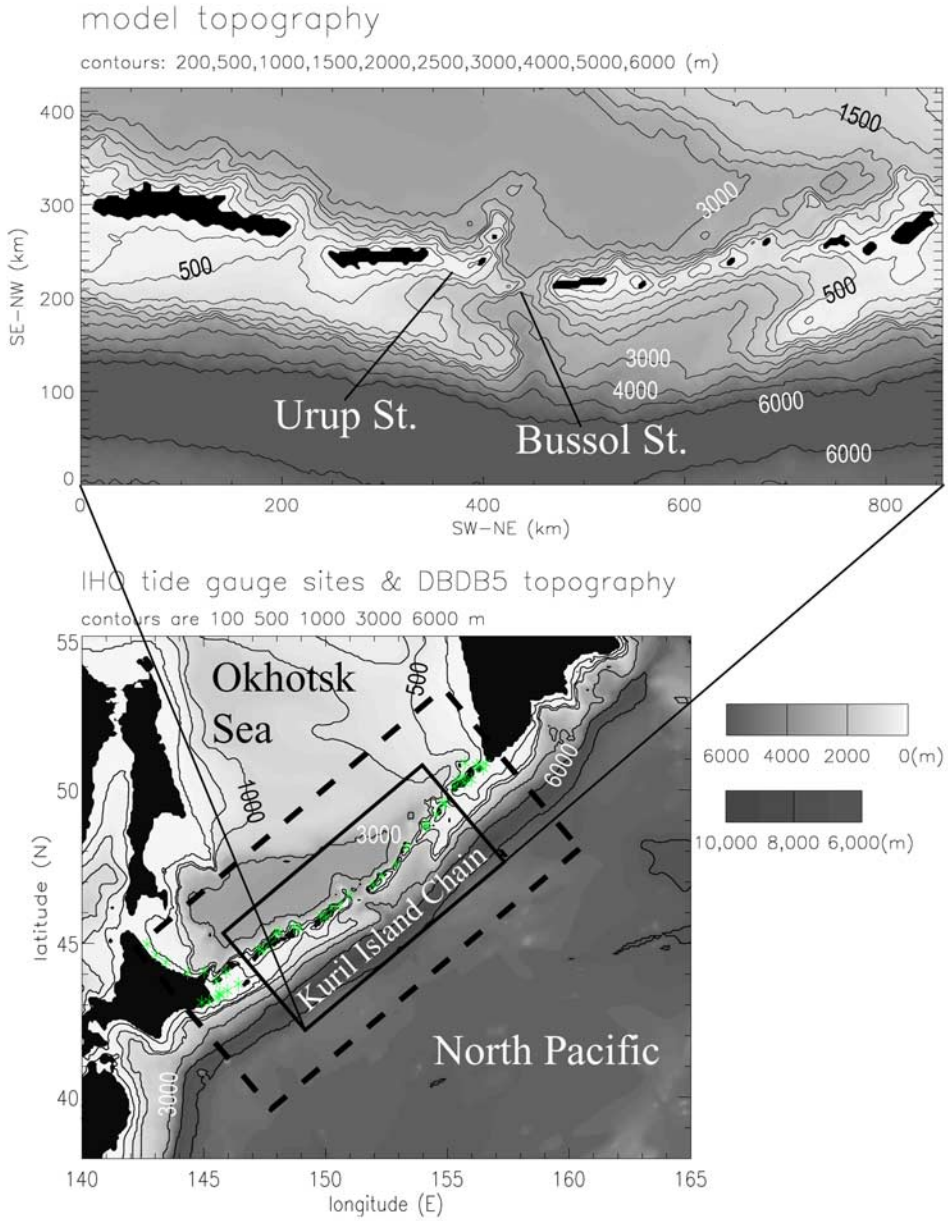

Figure 1. (top) Model topography. (bottom) Locations of the 3-D model domain (solid line) and the barotropic model domain (dashed line). The sites of tide gauge observations used in the comparison are shown by green asterisks in the bottom panel.

(∼1500 m) Straits. It is considered that the transport and mixing processes taking place between the Okhotsk Sea and the North Pacific via the Kuril Straits play an important role not only in the local environment but also in determining the water properties of the North Pacific [e.g., *Kitani*, 1973]. In turn, the North Pacific is the source of most of the water in the Okhotsk Sea [e.g., *Watanabe and Wakatsuchi*, 1998].

[3] Previous studies found that a plume of low-salinity water at 27.0 σ_θ extended to the south from the Kuril Straits and that the confluence of the East Kamchatka Current and the discharge from the Okhotsk Sea forms both the Oyashio current, which flows along the Kuril Islands as part of the western boundary current of the subarctic gyre, and the Subarctic Current to the east, thus indicating that the Okhotsk Sea is the most likely source of low-salinity water in the North Pacific [*Wüst*, 1930; *Favorite et al.*, 1976]. Associating an analysis of historical hydrographic data with *Kitani*'s [1973] result, *Talley* [1991] proposed that the North Pacific at mid-depth is ventilated through sea ice formation in the innermost part of the Okhotsk Sea and through local vertical mixing in the Kuril Straits. From potential vorticity (PV) maps, *Talley* [1993] and *Yasuda et al.* [1996] commented that the Okhotsk Sea supplies low-salinity water to the North Pacific Intermediate Water (NPIW). More exactly, the Okhotsk Sea Mode Water (OSMW), which is characterized by low potential vorticity around 26.8 σ_θ, is considered to be the major source of the NPIW [*Talley*, 1991; *Yasuda*, 1997; *Kono*, 1998; *Watanabe and Wakatsuchi*, 1998]. Since the NPIW spreads out over most of the subtropical gyre [*Talley*, 1993] and has the capacity to

store large amounts of greenhouse gases such as CO_2 [*Tsunogai et al.*, 1993; *Yamanaka and Tajika*, 1996], it is necessary to study the water transport and transformation processes taking place in the Kuril Straits.

[4] Recent observational results identified the importance of tidal processes at the Kurils in sustaining the interconnection between the Okhotsk Sea and the North Pacific. In fact, tidal currents, and especially their diurnal components, are very swift and predominant in and around the Kuril Straits [e.g., *Thomson et al.*, 1997] (see also Russian reports cited by *Talley and Nagata* [1995]). The maximum speed reaches 2 to 4 m s^{-1} in the relatively shallow straits (100 $\sim$ 500 m depth). According to previous studies on tidal rectification [e.g., *Huthnance*, 1973; *Awaji et al.*, 1980; *Robinson*, 1981; *Ridderinkhof*, 1989; *Chen and Beardsley*, 1995], such strong tidal currents induce significant mean transport, though the tidal flow itself is oscillatory. Moreover, observational studies in the northwest Pacific underlined the difficulty of explaining the in/outflow through the Kuril Straits in terms of geostrophic balance, because overall surface dynamic height is higher in the Okhotsk Sea than in the northwestern North Pacific [*Kawasaki and Kono*, 1992; *Isoguchi et al.*, 1997].

[5] Considering these facts, *Nakamura et al.* [2000a] (hereinafter NA00a) performed a numerical simulation of the barotropic tidal field in the Okhotsk Sea and showed that the diurnal K_1 tide induces very swift tidal currents in the Kuril Straits, as is observed. Since the K_1 tide is subinertial around this high latitude ($\sim$47°N), topographically trapped waves (TTWs) are effectively generated and amplified while circulating around the islands, a result expected on the basis of earlier theoretical studies [*Chapman*, 1989; *Haidvogel et al.*, 1993; *Kowalik and Proshutinsky*, 1995]. The work of NA00a indicated that the combined effect of vorticity transport by TTWs and vorticity advection by an oscillating tidal flow produces significant residual currents even in deep passages regardless of the weakness of the local tidal flow. The structures of the simulated tidally induced mean flows are similar to those reported in observations [*Leonov*, 1960], and the net transport toward the North Pacific due to the K_1 tide alone is estimated to be 5 Sv at least and more than 10 Sv from five major constituents.

[6] As for the transformation of water properties, recent detailed observations in the Kuril Straits have clearly revealed the presence of a deep, vertically uniform temperature distribution caused by a strong diapycnal mixing which leads to a horizontal discontinuity in the temperature distribution along the Kuril Islands [*Kawasaki and Kono*, 1994; *Gladyshev*, 1995; *Kawasaki*, 1996]. With a vertically two-dimensional (2-D) nonhydrostatic model, *Nakamura et al.* [2000b] (hereinafter NA00b) showed the importance of tidal mixing in the observed modification of water in the Kuril Straits. As swift K_1 tidal currents flow over sills in the Kuril Straits, unsteady lee waves are generated and grow into large-amplitude internal waves with a maximum displacement of $\sim$100 m. Though discussion of oceanic internal gravity waves generated by a tidal flow has usually focused on internal tides at the tidal frequency, the K_1 internal tides cannot exist as inertial gravity waves since the K_1 tide is subinertial in the Kuril Straits. Instead, unsteady lee waves can adopt this role and are more likely to grow by superposition than internal tides, so that enhanced diapycnal mixing to levels of diapycnal diffusivity $\sim$10–1000 cm^2 s^{-1} can eventually be reached [*Nakamura et al.*, 2000b; *Nakamura and Awaji*, 2001]. Such vigorous mixing takes place at the exit of the subducted OSMW and the entrance of the North Pacific water. Thus, from a dynamical viewpoint, these facts imply the supply of potential vorticity from the lateral boundary (i.e., the Kuril Island Chain) to both the North Pacific and the Okhotsk Sea, which could then affect the circulation of the adjacent Kuril Basin in the Okhotsk Sea and the subarctic gyre of the North Pacific according to the ventilated thermocline theory [*Pedlosky*, 1996]. Therefore, further investigation of the 3-D process of transport and diapycnal mixing at the Kurils with particular emphasis on the K_1 tide is required.

[7] In this study, we use a 3-D nonhydrostatic model. This model can reproduce shear instability and/or convective processes, which are important in vertical mixing induced by waves [*Scinocca and Peltier*, 1994]. Moreover, propagation of internal gravity waves and TTWs can be adequately simulated as well as currents in both along- and across-sill directions, thus enabling us to estimate the 3-D processes of tidally induced transport and diapycnal mixing reasonably and investigate the subsequent evolution of tidal fronts around the Kuril Island Chain. This knowledge will be helpful for clarifying the physics responsible for the linkage between the Okhotsk Sea and the North Pacific.

[8] The rest of the paper is organized as follows. The numerical model is described in section 2, and the results are presented in section 3. Section 4 presents an energy analysis, whereas diapycnal mixing is estimated in section 5. The offshore transport of the modified water by frontal eddies is estimated in section 6, and the roles of the eddy transport and tide-induced mean flow in the linkage between the Okhotsk Sea and the North Pacific are discussed in section 7. Our conclusions are summarized and discussed in section 8.

2. Model

2.1. Model Domain

[9] The model topography (Figure 1) is set from the DBDB5 topographic data (U.S. National Geophysical Data Center). The model domain covers most of the straits in the Kuril Island Chain so as to involve the two deep passages, the Bussol' and Kruzenshterna Straits, through which the major water flows are considered to take place, and to reproduce the propagation of TTWs and the tidally induced mean circulation around islands and/or sills. The two open boundaries along the island chain are set away from the straits to allow the evolution of eddies arising from tidal fronts. The model domain and its x and y axes are rotated anticlockwise by 45°. For computational efficiency, the model maximum depth is set as 6000 m so that the very deep region in the Kuril Trench is considered flat. Grid sizes are horizontally about 700 m and vertically 30 m (with the grid point dimensions of 1212 $\times$ 602 $\times$ 202).

2.2. Nonhydrostatic 3-D Model

[10] In order to simulate the baroclinic process induced by tides and the associated vertical mixing, we use a 3-D

nonhydrostatic model. This model is also suitable for representing the dispersion relation of internal gravity waves more accurately. Intense vertical mixing in and around the straits will bring about tidal fronts in the offshore region due to the difference in stratification, which evolve to produce pinched-off eddies by the frontal instability. Therefore we took into account the effect of a planetary-vorticity gradient by adopting the β-plane approximation. The model has been constructed using that of *Tanaka and Akitomo* [2001] as a basis, but with the following governing equations and settings:

$$\frac{\partial \mathbf{u}}{\partial t} + (\mathbf{u} + \mathbf{U}) \cdot \nabla \mathbf{u} + f\mathbf{k} \times \mathbf{u} = -\frac{1}{\rho_0}\nabla p - \frac{\rho}{\rho_0} g\mathbf{k} + \nu_H \nabla_H^2 \mathbf{u} + \nu_Z \frac{\partial^2 \mathbf{u}}{\partial z^2}, \tag{1}$$

$$\frac{\partial C}{\partial t} + \nabla \cdot [(\mathbf{u} + \mathbf{U})C] = \kappa_H \nabla_H^2 C + \kappa_Z \frac{\partial^2 C}{\partial z^2}, \tag{2}$$

$$\rho = \rho(\theta, S, p), \tag{3}$$

$$\nabla \cdot \mathbf{u} = 0, \tag{4}$$

where $\mathbf{u} = (u, v, w)$ are "internal mode velocities" in the (x, y, z) directions, respectively; $\mathbf{U} = (U, V, W)$ is a barotropic tidal flow; $\mathbf{k}$ is a unit vector along the z axis; p is pressure; ρ is density variation; and C represents potential temperature θ or salinity S. The equation of state is that recommended by UNESCO [*Jackett and McDougall*, 1995]. A pressure equation in the nonhydrostatic system is written in Appendix A.

[11] A barotropic tidal flow $\mathbf{U}$ is calculated separately from a barotropic tide model and is given in the advection terms that work as the main forcing (i.e., "surface lead assumption"). This separation allows us to greatly reduce the spin-up time and to circumvent difficulties in exact modeling of a free surface ocean for the nonhydrostatic equations [e.g., *Marshall et al.*, 1997a], and thus it is a convenient way to gain insight into important mechanisms before exploring a more accurate simulation. The detailed discussion on this assumption is given in section 8. Strictly speaking, the component $\mathbf{u}$ contains all the responses to the specified barotropic flow, but it is called here the "internal mode velocity," for convenience. Note that energy conversion through the Reynolds stress can cause feedback to the barotropic tide, but it is neglected for dynamical consistency with the surface lead assumption. Its effect is already included in the barotropic model in a crude manner as a result of using the bottom stress term and horizontal viscosity (more detailed discussion appears in section 8).

[12] The parameters are defined as follows: $f = f_0 + \beta_0 Y$ is the Coriolis parameter around 46.5°N ($f_0 \simeq 1.055 \times 10^{-4}$ s^{-1}, $\beta_0 \simeq 1.57 \times 10^{-13}$ cm^{-1} s^{-1}, and Y is the distance in the meridional direction; see Figure 1); ρ_0 is the reference density; g is the gravity acceleration; and ν and κ are the coefficients of eddy viscosity and eddy diffusivity, respectively, where the subscripts H and Z represent the horizontal and vertical directions.

[13] To reduce numerical diffusion associated with large vertical displacements by internal waves, the QUICK scheme [*Leonard*, 1979] is used in the vertical direction. The values of the eddy diffusivities are 0.1 cm^2 s^{-1} vertically and 10^4 cm^2 s^{-1} horizontally, and those of viscosities are 1 cm^2 s^{-1} and 10^5 cm^2 s^{-1}, respectively. These values are chosen from parameter-sweeping tests so as to be of the same order of those estimated from the calculated field, which will be shown in section 5.

[14] A no-slip condition is imposed at the bottom boundary. A sponge zone is adopted near the open boundaries to prevent artificial wave reflection, where the viscosities and the horizontal diffusivities are gradually increased. In addition, $\mathbf{u}$, θ, and S are gradually restored to their initial values near to the open boundaries, which, in effect, has the action of an artificial buoyancy flux and thereby maintains stratification in the interior.

2.3. Initial Conditions

[15] The initial potential temperature and salinity fields are set to be horizontally uniform with the vertical profiles shown in Figure 2 (green lines) using the data set of the U.S. National Oceanographic Data Center. In doing so, a summer time climatology in the Kuril Basin is used from the surface to 1500 m depth in order to examine the modification process of the Okhotsk Sea water entering the North Pacific. A summer time climatology of the East Kamchatka Current Water (EKCW) is used below 3000 m because the Kuril Basin (~3200 m depth) is shallower than the deep part of the Pacific region, and because it is the origin of the water in this region [*Reid*, 1965]. To avoid a vertical gap in density around 3000 m depth, the initial vertical profiles of θ and S are gradually changed from the climatology of the Kuril Basin to that of the EKCW between 1500 m and 3000 m depth. Note that at these depths the difference in stratification between the two climatology profiles is small (Figure 2). As stratification in summer becomes strong, a significant amount of the energy contained in internal waves could be trapped in a "surface" layer, which may reach down to ~100 m depth. The initial internal mode velocity is set to be zero, and thus only the barotropic tidal flow is taken into account for the initial velocity field.

2.4. Barotropic Tidal Flow

[16] In this experiment, we direct our attention to the K_1 tide alone since the K_1 current is largest around the Kuril Island Chain [e.g., *Thomson et al.*, 1997; *Nakamura et al.*, 2000a]. The barotropic tide model used here is the same as that of NA00a and is based on work by *Schwiderski* [1980]. The horizontal resolution, however, is taken to be the same as in this 3-D model and hence is about 7 times finer than that used by NA00a. In addition, the model domain of the barotropic tide is wider than that of the present 3-D model in order to reduce spurious disturbances at the open boundaries of the 3-D model as much as possible (Figure 1). The basic features of the calculated barotropic field are essentially the same, but with increasing horizontal resolution, the accuracy improves.

[17] For example, using the International Hydrographic Office tidal harmonic constants at 43 sites, as shown in

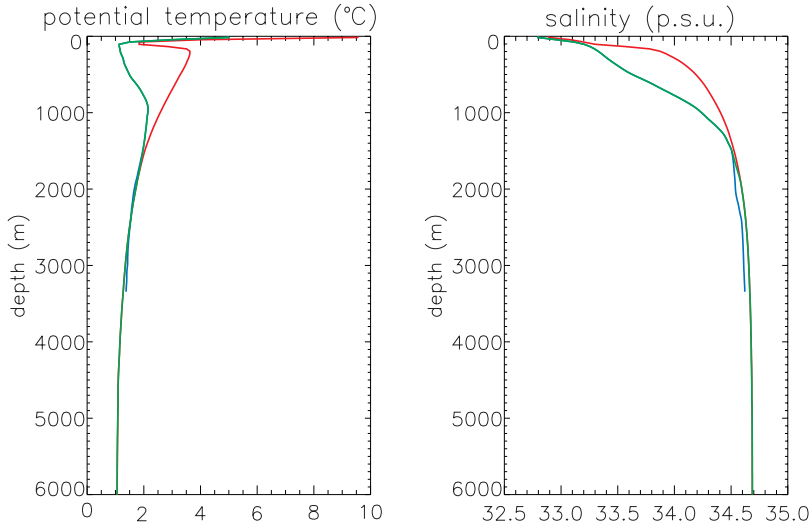

Figure 2. Initial vertical profiles of (left) potential temperature and (right) salinity are shown by green lines. The blue and red lines are those of summer time climatology in the Kuril Basin of the Okhotsk Sea and the East Kamchatka Current, respectively.

Figure 1, we calculate the root mean square (RMS) misfit of elevation as per NA00a. The RMS misfit is 6.37 cm, while the mean observed amplitude is 30.3 cm. The correlation coefficients between the calculated and the observed harmonic constants are 0.73 for phase and 0.76 for amplitude. These values are reasonably good despite the complex topography, so that the simulation is considered to be realistic.

[18] The simulated K_1 barotropic flow is very rapid in shallow regions and hence strong wave generation is expected to occur (Figure 3). This is particularly so in the vicinity of topographic features such as sills and banks, where the maximum speed exceeds 2 m s^{-1}. In the Bussol' Strait, the flow speed ranges from 0.13 m s^{-1} in the deepest part to 0.5 m s^{-1} over the western sill. These values are similar to the values of 0.3–0.4 m s^{-1} derived from satellite-tracked drifters [*Ohshima et al.*, 2002]. Around the Friz (Etorofu) Strait, the simulated speed varies from 0.3 to 1 m s^{-1}, in good agreement with the estimation from satellite-tracked drifters by *Thomson et al.* [1997] and *Rabinovich and Thomson* [2001]. As for the shallow straits, where only Russian observations have so

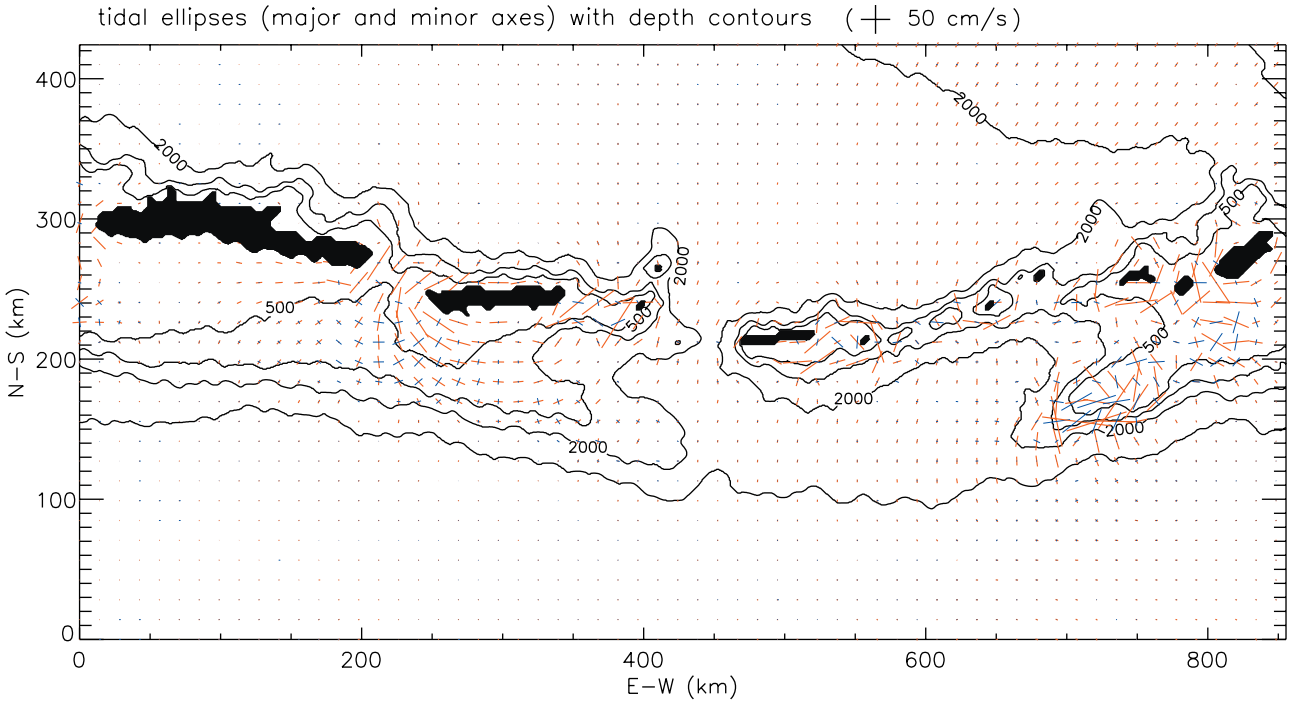

Figure 3. Major (red) and minor (blue) axes of the calculated barotropic K_1 tidal flow. Horizontally averaged values over every 20 × 20 grid points are shown. Depth contours at 500, 1000, 2000, and 4000 m are overplotted.

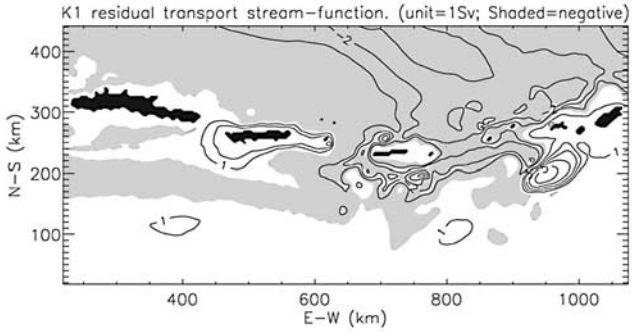

Figure 4. Eulerian mean transport stream function for the barotropic K_1 tide, which is set to be zero at Hokkaido Island. Values in shaded areas are negative. The contour interval is 1 Sv (contours of 0 Sv are excluded).

far been permitted, the Luchin report from *Talley and Nagata* [1995] commented on the presence of very strong currents of 5 to 7 knots. Generally speaking, the agreement obtained between the simulated and observed parameters support the view that our numerical simulation for the K_1 tidal current field is realistic.

[19] As mentioned by NA00a, significant TTWs are readily excited as the subinertial K_1 tidal waves coming from the North Pacific encounter the large-amplitude sills in the Kuril Straits. TTWs intensify the K_1 current, leading to the generation of a remarkable tidally induced mean flow (Figure 4) through the "extended tidal rectification" proposed by NA00a. In Figure 4, a "bi-directional" residual flow structure is clearly present in the straits in addition to circulation around shallow topographic features like islands and sills as reported by *Moroshkin* [1966] and NA00a. Some eddy-like features also appear in this fine-resolution case.

3. Features of the Simulated Field

3.1. Tidal Fronts and Eddies

[20] Figure 5a shows the model sea surface temperature after 25 periods (after an interval of time corresponding to 25 periods). Low temperature anomalies are produced along the island chain, which indicate the formation of tempera-

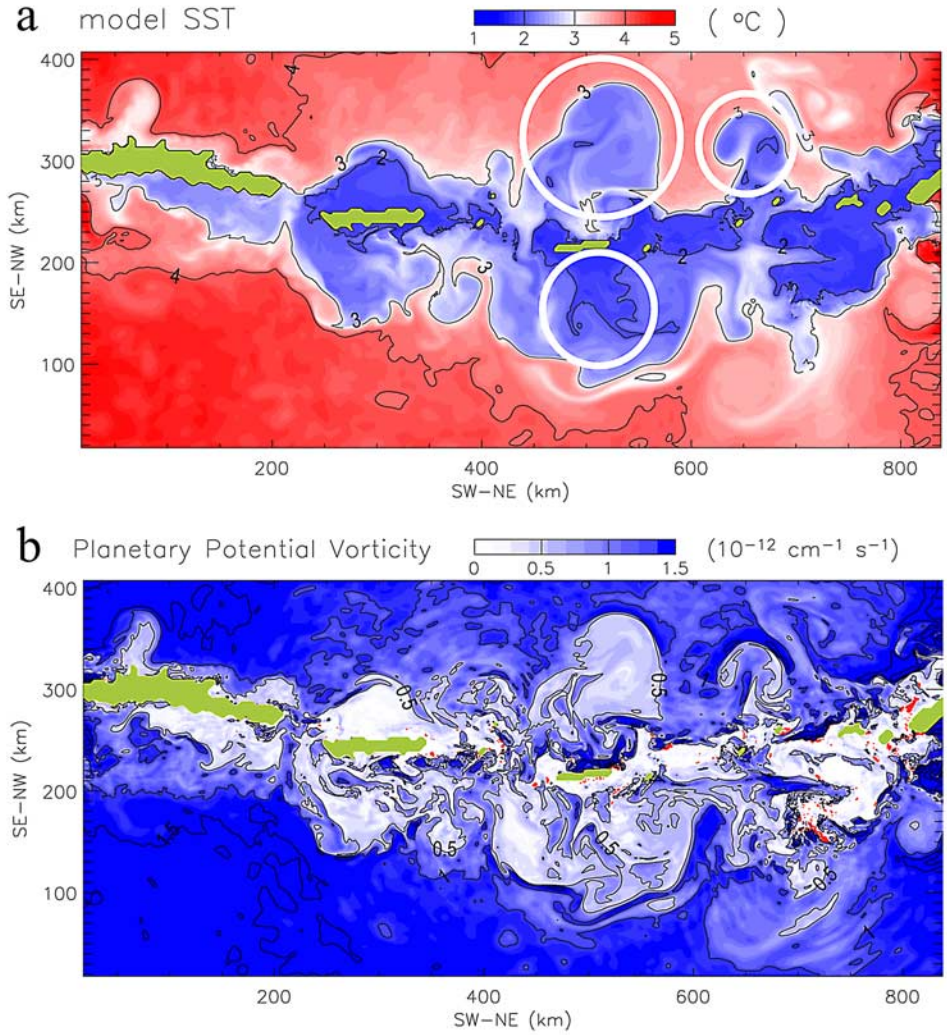

Figure 5. (a) Temperature at the model sea surface (15 m depth) after 25 periods. Green areas indicate lands. White circles indicate eddy-like structures also seen in a satellite-derived sea surface temperature imagery (Figure 6). (b) Planetary part of potential vorticity ($-f/\rho_0 \times d\sigma_\theta/dz \times 10^{-3}$) after 25 periods at 30 m depth. In Figure 5b, red color areas indicate density inversion.

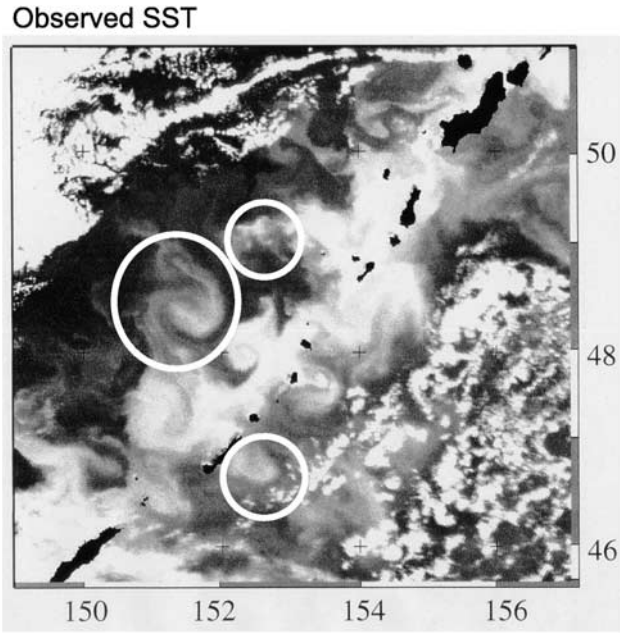

Figure 6. Satellite-derived sea surface temperature (MCSST/AVHRR) over the northern part of the Kuril Straits from the NOAA-12 satellite (orbit 17429; time 2231–2233 GMT; 21 September 1994). White circles indicate eddy-like structures similar to features in the model SST (Figure 5). Note that the model domain is inclined by 45°. (Figure courtesy of S. Saitoh)

ture fronts and eddies. The patterns and size of eddies are generally similar to those seen in an infrared imagery (Figure 6). In particular, the eddy-like structures marked by white circles take place at almost the corresponding locations and bear a resemblance. Such temperature fronts are known to exist almost throughout the year, although cooling in winter makes it a warm anomaly [*Kitani*, 1973]. These facts strongly suggest that tidally induced baroclinic processes are responsible for the observed fronts and eddies.

[21] Since the formation of tidal fronts are associated with vertical mixing and/or stirring [e.g., *Simpson et al.*, 1978; *Nakamura et al.*, 2000b], we next examine the planetary component of potential vorticity, $-\frac{f}{\rho_0}\frac{\partial \rho|_{p=0}}{\partial z}$ (PPV), which is a useful indicator of water mass transformation by diapycnal mixing. Though fronts can be also identified by potential energy anomaly, since we set the initial stratification to be horizontally uniform, the change in PPV implies the presence of available potential energy. A vertical distribution of potential density and PPV after 25 periods over a sill in the northeastern part at x = 575 km (Figure 7) indicates that water mass transformation occurs over the sill from the sea surface to the intermediate layer. Low PPV water is produced over the sill though it shifts somewhat to the right from the sill due to advection. Several previous observations confirmed the presence of such vertically uniform water masses in the northeastern part of the Kurils [*Gladyshev*, 1995; *Kawasaki*, 1996] as well as in the Bussol' Strait [e.g., *Kitani*, 1973; *Kawasaki and Kono*, 1994]. Beneath this low PPV component, high PPV water is produced around 27.1 σ_θ, mainly because of entrainment of the water into the above layer (thus layer thickness decreases). A similar situation occurs above the low PPV water, though it is not clearly appreciable. Figure 7 also shows the presence of density inversions (denoted by red) between the surface and intermediate layers (say, 26.9 σ_θ to 27.3 σ_θ), thus indicating that water mass transformation is still going on. Such PPV change indicates that the temperature fronts are caused by tidal mixing, considering the fact that the initial condition is horizontally uniform.

[22] The formation of PPV fronts is due to the fact that the vertical mixing taking place in and around the sills or islands is stronger than that in the surrounding deep regions. The fronts, in turn, spawn various instabilities such as baroclinic instability and associated eddies [e.g., *Qiu et al.*, 1988; *Boss and Thompson*, 1999; *Pedlosky*, 1987]. Figure 5b shows that the sea surface PPV map after 25 periods clearly corresponds to the modeled temperature distribution. The tidally induced PPV fronts evolve by forming and releasing baroclinic eddies. These eddies should contain low PPV water in their cores, and thus anticyclonic eddies are easier to produce. A very recent hydrographic observation in the Kuril Basin, which was

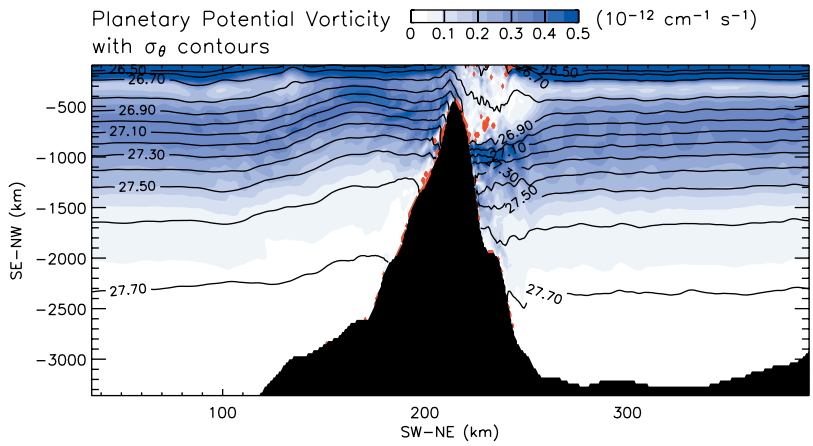

Figure 7. Vertical section of planetary part of potential vorticity ($-f/\rho_0 \times d\sigma_\theta/dz \times 10^{-3}$: tone) and potential density (σ_θ: contour) after 25 periods. The section crosses a typical sill in the northeastern part of the Kuril Island Chain (x = 575 km). Red color areas indicate density inversion.

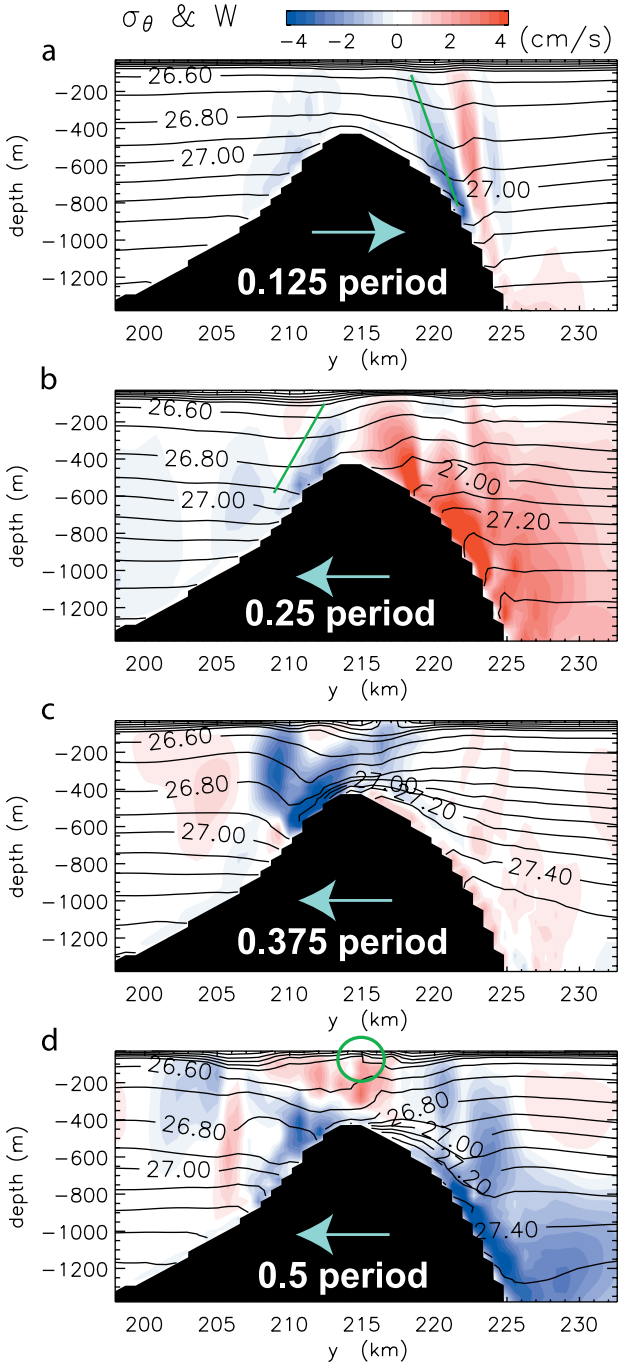

Figure 8. Initial evolution of potential density (σ_θ: contour) and vertical velocity ($w + W$: tone) in a y-z section across a sill (the same one in Figure 7). Contour interval is 0.1 σ_θ. Arrows in the sill region represent the direction of the across-sill barotropic flow. Green lines denote the waves whose intrinsic frequencies are estimated in Table 1.

carried out by a Hokkaido University group, clearly captured such a pinched-off eddy originating from the Kuril Straits (M. Itoh, personal communication). This indicates that eddies convey vertically well-mixed water located around the straits toward the offshore region. We will return to this aspect in section 6.

[23] According to NA00b, unsteady lee waves generated over sills at the Kurils are more likely to induce intense vertical mixing. Thus we next examine wave processes in order to shed light on the mechanism responsible for water mass transformation in the Kuril Straits.

3.2. Generation of Unsteady Lee Waves

[24] Figure 8 shows the initial response of isopycnal surfaces and vertical velocities over the sill located in the northeastern part to the barotropic K_1 flow. This cross section corresponds to that of the PPV discussed above, and an internal wave response is easy to identify because the sill is relatively wide.

[25] Figure 8a shows that as a barotropic across-sill current flows rightward, an internal wave-like structure is generated on the lee side of the sill. The co-phase lines lean toward the upstream side, thus indicating that the wave is an unsteady lee wave. In fact, the subinertial K_1 internal tide cannot exist as inertial gravity waves. Even for a simple higher harmonics like K_2, such waves should propagate in both upstream and downstream directions, in contrast to the result simulated here.

[26] The intrinsic frequency of internal waves is estimated from the simple dispersion relation,

$$\sigma_i^2 = \frac{N^2(\lambda_v/\lambda_h)^2 + f^2}{1 + (\lambda_v/\lambda_h)^2}, \tag{5}$$

where λ_v/λ_h is the ratio of vertical and horizontal wavelengths, σ_i is an intrinsic frequency, and N is a buoyancy frequency. When we use the approximation of $\lambda_h^{-2} \sim k_c^2/4\pi^2$ (where k_c is the horizontal wave number in the across-sill direction), the frequency estimated from the figure (Table 1) roughly agrees with the theoretically predicted frequency of unsteady lee waves: According to NA00b, the intrinsic frequency of tidally generated internal waves is, in general, given as

$$k_c v_c \pm \sigma_{K1}, \tag{6}$$

where v_c is the across-sill current speed and σ_{K1} is the K_1 tidal frequency. Though unsteady lee waves can be excited when $|k_c v_c/\sigma_{K1}| \gg 1$ in their definition, the behavior of the waves becomes similar to that of unsteady lee waves when $|k_c v_c/\sigma_{K1}| > 2$ as in this case [*Nakamura and Awaji*, 2001]. For this reason, in the following discussion, we use the

Table 1. Estimate of Intrinsic Frequency[a]

Period	$2\pi/k_c$	λ_v/λ_h	v	Dispersion Relation	Unsteady Lee Wave
1/8	6 (±0.5) km	0.17 (±0.02)	31 (±5) cm/s	4.8 (±0.8) × 10^{-4} s^{-1}	4.0 (±0.8) × 10^{-4} s^{-1}
1/4	4.5 (±0.5) km	0.14 (±0.02)	19 (±5) cm/s	4.0 (±0.8) × 10^{-4} s^{-1}	3.4 (±1.0) × 10^{-4} s^{-1}

[a]Values of $2\pi/k_c$ and λ_v/λ_h are estimated from Figure 8. The buoyancy frequency used is the vertical average from 150 m to 1000 m at the initial time (2.8 (±0.2) × 10^{-3} s^{-1}) and the across-sill velocities used are the barotropic flows 1/16 period before the corresponding times. The theoretically predicted frequency of an unsteady lee wave shown is that of the fast mixed tidal−lee wave component only [*Nakamura and Awaji*, 2001]. A range of possible errors in estimating each value is indicated in brackets.

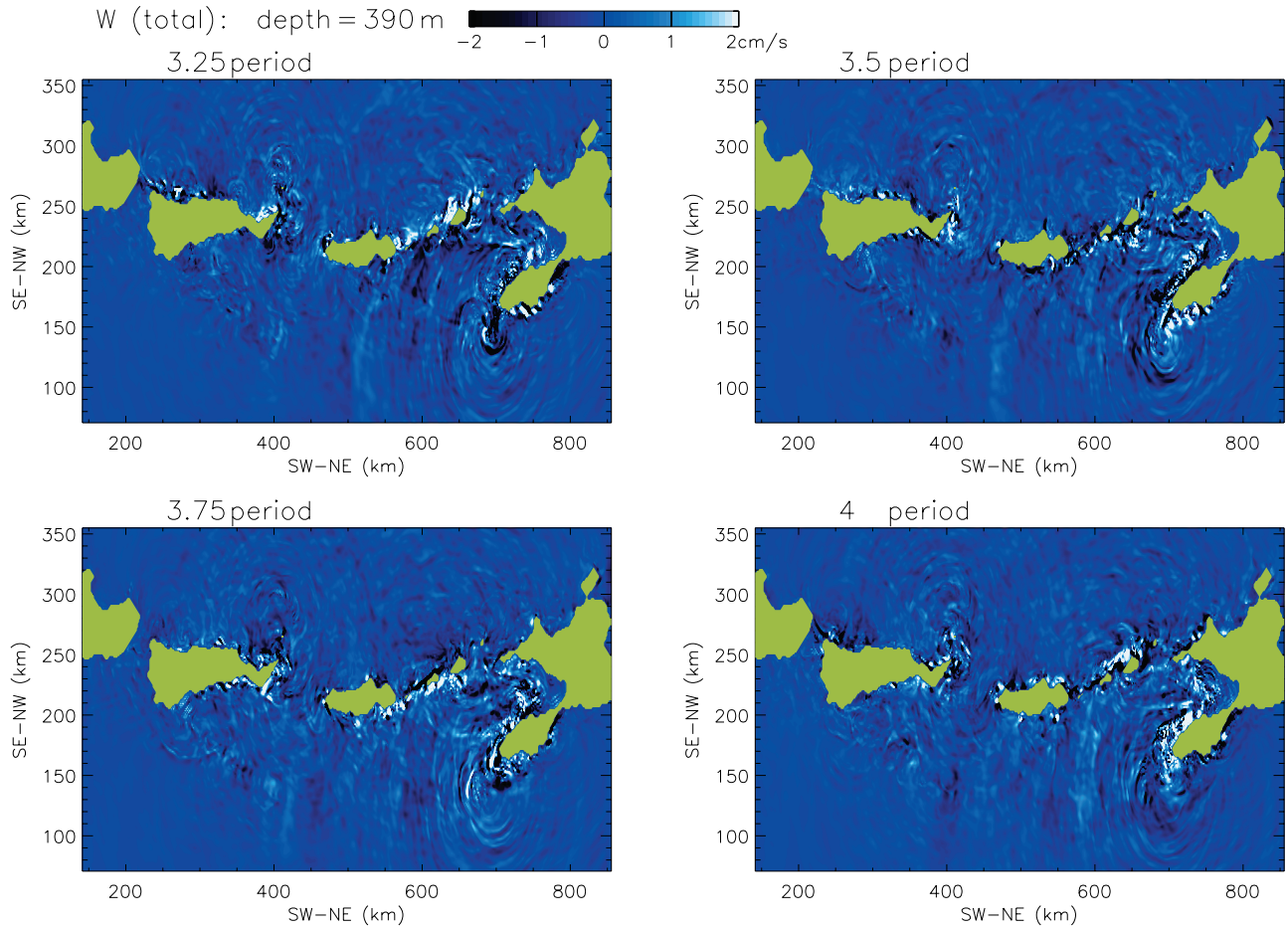

Figure 9. Horizontal sections of total vertical velocity in the fourth period at 390 m depth, which approximately corresponds to that of the OSMW (and thus NPIW) core. Green areas indicate land grids at this depth.

name unsteady lee waves in a broader sense than the original definition for convenience.

[27] After 1/4 period (Figure 8b), the across-sill flow turns to the left and another unsteady lee wave is generated over the left side of the sill top. The unsteady lee wave produced by rightward flow in the previous period begins to propagate to the left as the across-sill flow weakens and reverses its direction. After 3/8 period, superposition of a propagating unsteady lee wave and a newly generated unsteady lee wave evolves into a large-amplitude wave with a displacement of about 200 m (Figure 8c). Such amplification eventually causes significant wave breaking, which then leads to strong diapycnal mixing even though the barotropic flow is not so strong here (the amplitude is about 60 cm s^{-1}).

[28] These features are qualitatively similar to those in the vertically 2-D case (NA00b). However, the responses around islands and/or banks are more complicated due to 3-D wave processes such as waves propagating from other sills and their reflection at islands and to more complex features in the flow field. In addition, in the case of a strong barotropic tidal flow passing over a sill, strongly nonlinear phenomena like bores and intense bottom currents accompanying strong vertical shear can occur and give rise to considerable mixing across the wider density range from 26 σ_θ to 27.6 σ_θ (not shown). In this way, water masses are transformed in and around the Kuril Straits. More detailed estimates will be presented in section 5.

3.3. Horizontal Distribution of Unsteady Lee Waves

[29] A signature from internal waves is easily visible in vertical velocity. Figure 9 shows the horizontal distribution of vertical velocity simulated for the fourth period at 390 m depth, roughly corresponding to the core density layer of NPIW. Many large-amplitude waves are present in Figure 9 and can be identified as inertial gravity waves from their spreading pattern and speed. The generation mechanism of these waves is inferred to be unsteady lee wave (and/or mixed tidal lee wave) excitation from the same reasons as discussed in the previous section. In short, large-amplitude unsteady lee waves are produced all along the Kuril Island Chain.

[30] Though these waves interfere with each other all over the domain, a surface of constant phase must indicate a generation region. A close examination reveals that large-amplitude internal waves originate mainly from (1) the bank located in the northeastern Pacific region (around x = 700 km and y = 150 km), (2) the Urup Strait, and (3) sills in the northeastern part of the island chain. These regions are characterized by low PPV and temperature anomalies in Figure 5. Therefore it is inferred that one of the main causes of intense vertical mixing in the Kuril Straits results from the generation of large-amplitude unsteady lee waves.

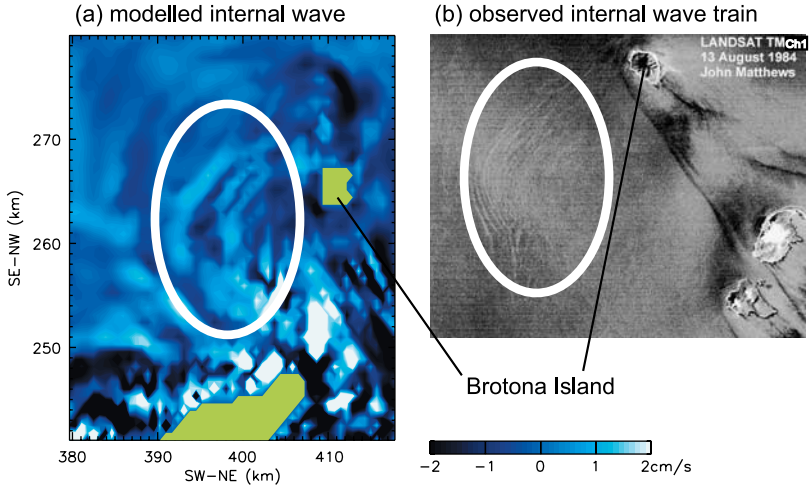

Figure 10. (a) Same as Figure 9 but for the north of the Urup Strait after 3.875 period. (b) An observed internal wave train identified in the visible band channels of a LANDSAT-4 image gathered on 13 August 1994. (Figure courtesy of John Matthews). The circles indicate the waves in the corresponding region.

[31] Another interesting feature in the model result is that a propagating wave train is observed north of the Urup Strait as marked in Figure 10. Some evidence of a corresponding effect in nature is present in a LANDSAT-4 image (Figure 10) gathered on 13 August 1984 (the mechanism through which ocean internal waves become visible on radar and/or visible-band images is discussed, for example, by *Apel et al.* [1975] and *Alpers* [1985]). Here the 30-m spatial resolution offered by the visible band channels enables a soliton-like wave train propagating in the almost same direction at the same location to be provisionally identified. The difference in wave number is attributed to a limited model resolution, which weakens the disintegration process of large-amplitude internal waves. Though we cannot state with certainty that this wave-like feature is generated by a subinertial diurnal tide because of the limited data availability, the close similarities outlined here support the possibility of generation by the strong Kuril Islands tides.

[32] Some of these waves travel long distances and gradually decay. For example, large-amplitude waves propagate from the Urup Strait to the Bussol' Strait. Also, waves propagating from the bank in the Pacific region (x = 700 km and y = 150 km) reach Urup Island. Considerable energy transport by these waves could supplies energy for mixing along the pathways, even in deep passages.

3.4. Topographically Trapped Waves

[33] In addition to the unsteady lee waves described above, a tidal flow over a slope can excite internal tides at the corresponding tidal frequency. Since the K_1 tide is subinertial in the Kuril Straits, K_1 internal tides are topographically trapped, whereas unsteady lee waves (and mixed tidal lee waves) can exist as inertial gravity waves, as summarized in Table 2. For the effective detection of TTWs, we consider along-isobath velocity data at the model sea surface (Figure 11). In general, TTWs exhibit their signal strongly in along-isobath velocity, and the surface is not a node in the vertical direction. Subinertial TTWs are rotational (except for Kelvin waves), and hence the rotary spectral is often used for detection [e.g., *Hsieh*, 1982; *Cummins et al.*, 2000]. Here, however, relative vorticity parameter is not so good because the dominant contribution comes from inertial gravity waves.

[34] Figure 11 shows clockwise propagation of both baroclinic and barotropic components around topographic features. Examples are indicated using red and black arrows for positive anomalies of the baroclinic and barotropic components, respectively (a positive along-isobath flow is defined as the flow with the shallower water on the right). A careful look at these arrows points to a difference in phase speed and thus in phase between these two components. This confirms that baroclinic signals are not merely forced motions and are associated with baroclinic TTWs. Similar wave propagation is detected in recent observations [*Rabinovich and Thomson*, 2001]. Note that positive anomalies are stronger than negative ones in most places. This fact suggests that clockwise mean flows around islands are produced by TTWs as discussed by NA00a, though both barotropic and baroclinic components are involved in this case. For this reason, the mean flows produce the "bi-directional"

Table 2. Properties of Tidally Generated Internal Waves[a]

	$kU_0/\sigma_{tide} \gg 1$	$kU_0/\sigma_{tide} \sim 1$	$kU_0/\sigma_{tide} \ll 1$
Wave type	unsteady lee waves	mixed tidal lee waves	internal tides
Intrinsic frequency	$\sim -kU(t)$	$-kU(t) \pm \sigma_{tide}$	$\sim \pm\sigma_{tide}$
When $\sigma_{tide} < f$	internal gravity waves (IGW)	IGW and/or TTW	topographically trapped waves (TTW)
Propagation	capable of crossing isobaths	cross and/or along a slope	(clockwise) along a slope

[a]Here σ_{tide} is the tidal frequency, k is horizontal wavenumber (or curvature of the topography), and U_0 is flow speed amplitude. For details, please see *Nakamura and Awaji* [2001].

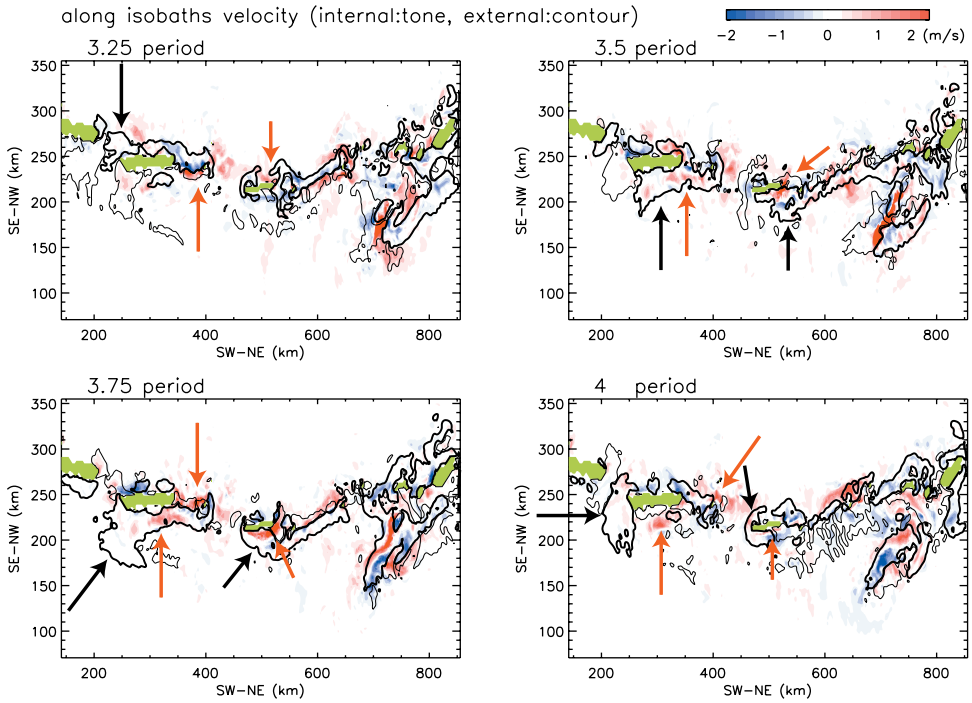

Figure 11. Along-isobath velocity of the internal mode (color) and the barotropic (contours) components in the fourth period at the model sea surface (15 m depth). Positive is defined as the direction with the shallower water on the right. Contours for the barotropic component are drawn at 20 cm s^{-1} (thick line) and −10 cm s^{-1} (thin line).

current structure within the straits leading to effective tidal exchange as shown in section 7.

4. Energy Analysis

[35] As described in the previous section, subinertial K_1 internal tides take the form of TTWs and propagate along the slope, whereas unsteady lee waves behaving as inertial gravity waves in nature can propagate across the slope. Horizontal propagation of these two kinds of waves could be accompanied by energy transport from energetic wave-generation regions (i.e., shallow sills) to deep regions. In particular, when generated in the shallow Urup Strait of swift barotropic flow, both types of wave can convey considerable energy to the adjacent deep Bussol' Strait where weak barotropic forcing is present. This possibility is examined below.

4.1. Energy Equation

[36] The equation used in an energy analysis is

$$\frac{\partial E}{\partial t} + C_{APE} = -\nabla \cdot [(\mathbf{u} + \mathbf{U})E + \mathbf{u}p] + \rho|'_{p=0} gW + D, \qquad (7)$$

where

$$E = KE + APE, \qquad (8)$$

$$KE = \frac{1}{2}\rho_0 \mathbf{u} \cdot \mathbf{u}, \qquad (9)$$

$$APE = \frac{1}{2}\frac{g^2 \rho|'^2_{p=0}}{\rho_0 \overline{N^2}|^{xyt}_{p=0}}, \qquad (10)$$

$$C_{APE} = \frac{APE(w+W)}{\overline{N^2}|^{xyt}_{p=0}} \frac{d}{dz}\left(\overline{N^2}|^{xyt}_{p=0}\right) + \left(\rho' - \rho|'_{p=0}\right) gw, \qquad (11)$$

$$\overline{N^2}|^{xyt}_{p=0} = -\frac{g}{\rho_0}\frac{d}{dz}\left(\overline{\rho}|^{xyt}_{p=0}(z)\right). \qquad (12)$$

Here $\overline{\rho}|^{xyt}_{p=0}(z)$ is a horizontal average of the time-averaged potential density over a cycle and $\rho|'_{p=0}$ is the deviation from it. Total energy, E, is the sum of kinetic energy of the internal mode, KE, and the available potential energy, APE, defined following *Gill* [1982]. Basically, energy is supplied from the barotropic tidal flow to APE through the conversion term $\rho|'_{p=0} gW$. The term C_{APE}, arising from the vertical variation of $\overline{N^2}|^{xyt}_{p=0}$ and the compressibility, can be interpreted as a correction term. A detailed discussion is made in Appendix B. The right-hand side of equation (7) consists of the convergence of energy flux arising from the advection and the work by pressure, together with the local energy supply and a dissipation term D.

4.2. Energy Flux and Supply

[37] Figure 12 shows the depth-integrated energy flux vectors and potential energy supply. To focus on the horizontal energy transport during one tidal period, these data are temporally averaged over the fourth period. It should be noted that around this time, the wave spin-up process is largely at an end as seen in Figures 9 and 11.

[38] The potential energy supply from barotropic flow is quite large around the bank and sills in the northeast region and around the Urup Strait. These are areas where large-amplitude unsteady lee waves are generated, as indicated in

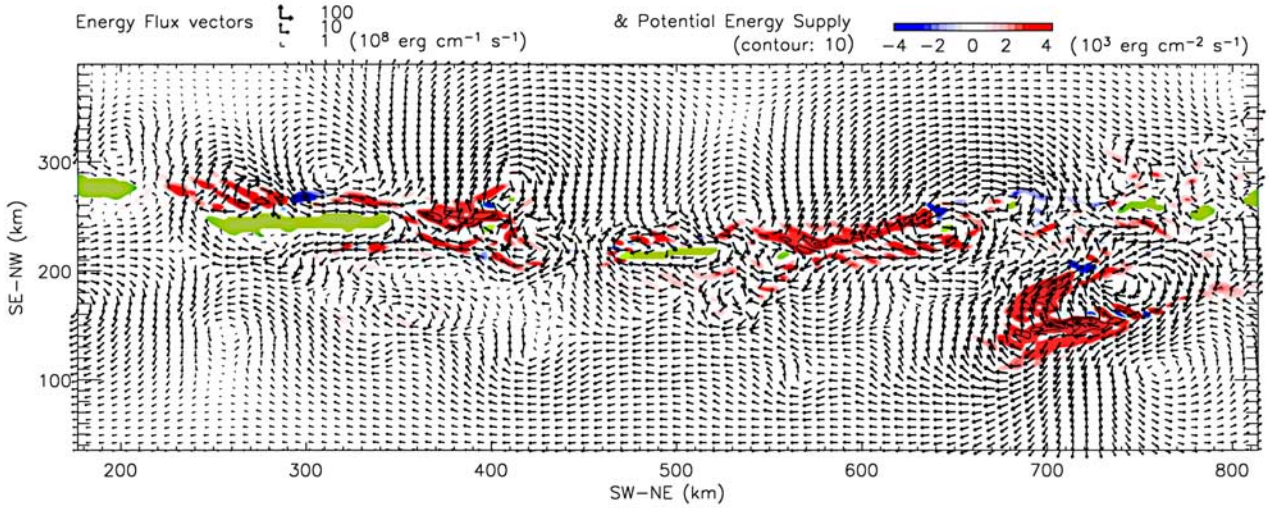

Figure 12. Energy flux vectors superposed on the distribution of potential energy supply from the barotropic tidal flow, which are vertically integrated and temporally averaged in the fourth period. Arrows are plotted at every 10 grid points and represent the horizontal average over 10 × 10 grids. Contours are also drawn at intervals of 10×10^3 erg cm^{-2} s^{-1}.

the preceding section. This fact therefore confirms that a large amount of energy is transported from these wave generation regions. Figure 12 implies that the energy transport can be primarily attributed to both an across-isobath energy flow carried by inertial gravity waves and to a clockwise along-isobath transport carried by TTWs. Interestingly, the across-isobath flux also moves in a clockwise sense. This is mainly because unsteady lee waves generated by a clockwise barotropic flow propagate in a clockwise sense and hence draw spiral trajectories. Therefore the wave energy flux from the Urup Strait to the Bussol' Strait is intensified. This takes place in the western part of the strait, with a similar process developing in the east.

[39] The term balances of equation (7) in the fourth period in the Bussol' and Urup Straits are shown in Table 3. It is clear that energy influx from outside regions dominates in the deep Bussol' Strait (even after it is largely canceled by outflux). This is made mainly through the work done by the pressure term and therefore comes from the energy transport by waves. Since dissipation acts on both waves and the mean state, the dissipation term also becomes dominant when temporally averaged. This therefore implies that incoming waves lose their energy in this region to small-scale turbulent motions leading to diapycnal mixing.

[40] On the other hand, the local energy supply from the barotropic tide is even smaller than the energy increase rate ($\partial E/\partial t + C_{APE}$). This also indicates the importance of the net energy influx by waves propagating from adjacent shallow sills. Though this small fraction of energy input, which is now used to increase the local energy, will be consumed by dissipation and/or outflux after the energy increases to a saturation level, the main balance is not affected qualitatively.

[41] In contrast, the energy balance in the shallow Urup Strait shows that energy derived from the barotropic flow is distributed out to the adjacent deep regions. Though the presence of large-amplitude waves makes the correction term somewhat large, it is not a dominant term.

5. Diapycnal Mixing

5.1. Method

[42] To estimate the intensity of vertical mixing associated with the wave generation and energy transport processes, we calculate diapycnal diffusivity coefficients, K_ρ, using the data in the fourth period. In doing so, since the periods of unsteady lee waves are much different from the tidal period, the diffusivity coefficients will be overestimated when calculated on the basis of the Fickian formulation (i.e., $K_z = \overline{\rho' w'}/(\partial\overline{\rho}/\partial z)$, where $\overline{()}$ and $'$ denote a temporal average over one tidal period and its deviation, respectively). In fact, the calculated values (not shown) were about 10 times larger than those shown later, though the overall pattern was similar.

Table 3. Energy Budget in the Fourth Period[a]

Strait	$\partial KE/\partial t$	$\partial APE/\partial t$	C_{APE}	$-\nabla \cdot [(\mathbf{u}+\mathbf{U})\mathbf{E}]$	$-\nabla \cdot (\mathbf{up})$	$\rho\|_{p=0}' gW$	Dissipation
Bussol' ($\times 10^{15}$)	0.92	1.26	−0.82 + 0.14	0.88	4.60	1.41	−5.39
Urup ($\times 10^{16}$)	−0.01	0.03	1.21 + 0.03	−1.09	−2.58	5.78	−0.85

[a]Values shown are volume-integrated and time-averaged values for the fourth period. The integration regions are (x = 430 km, 460 km, and y = 190 km, 230 km) for the deep "Bussol' Strait" and (x = 360 km, 390 km and y = 210 km, 270 km) for the shallow "Urup Strait." The unit is erg cm^3 s^{-1}. The dissipation is calculated as the residual of the other terms. The values of the correction term are shown for both the first and second terms in equation (11).

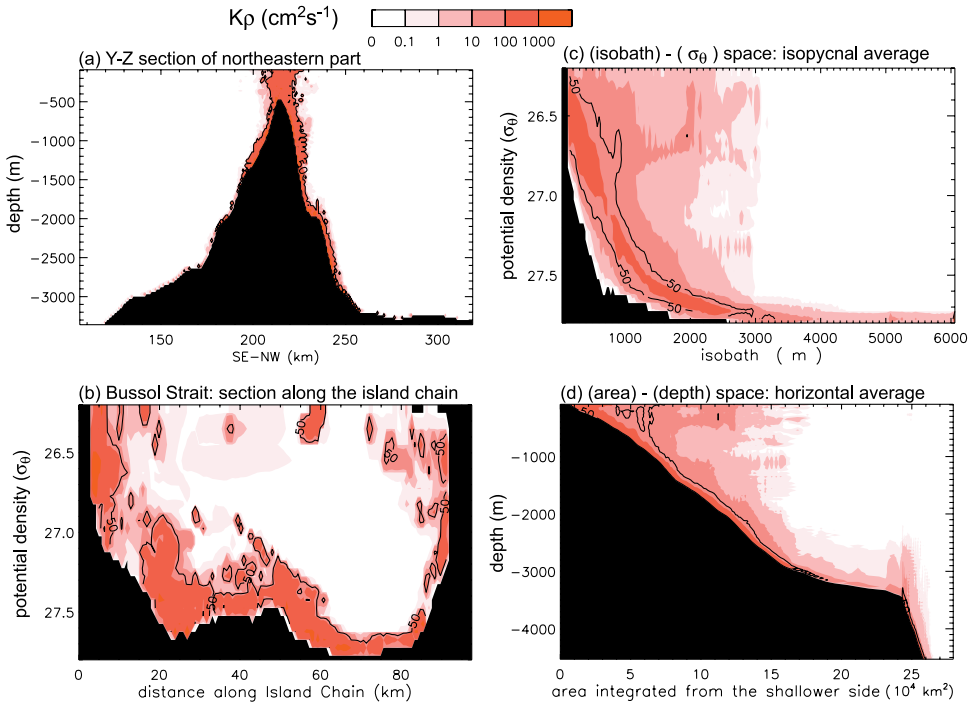

Figure 13. Temporally averaged diapycnal diffusivity coefficients ($cm^2\ s^{-1}$) estimated from the calculated fields in the fourth period. Contours are drawn at 50 $cm^2\ s^{-1}$. (a) An example of y-z sections across a moderately high sill (the same one in Figure 7). (b) The Bussol' Strait section shown along the Island Chain, but the vertical axis is potential density. (c) Average along isobaths taken on isopycnal surfaces. Vertical and horizontal axes are σ_θ and isobaths, respectively. (d) Average along isobaths but on the horizontal surfaces. The abscissa represents the area integrated from the shallower side, and ordinate is depth. The depth at the bottom of the averaged values (the top of the black area) corresponds to the depth of the isobath along which the average is taken.

[43] Thus we estimate the diffusivity using the following scaling proposed by *Gregg* [1989]. Since the method is based on the internal wave dynamics and observations, it allows us to estimate the diapycnal diffusivity more accurately in the presence of waves of various frequencies. Although *Polzin et al.* [1995] indicated that *Gregg*'s [1989] parameterization can result in underestimates of energy and thus its dissipation rate, ϵ, in a high energy region and hence proposed a more sophisticated scaling, it is difficult to apply their method to our model results because of the huge data size.

[44] Owing to our limited grid size, a 30-m shear is used instead of the 10-m shear of *Gregg* [1989] for the estimation of ϵ and dynamical mixing coefficient, K_ρ as

$$\epsilon = 7 \times 10^{-10} \frac{N^2}{N_0^2} \frac{S_{30}^4}{S_{GM}^4}, \tag{13}$$

$$K_\rho = 0.25 \frac{\epsilon}{N^2}. \tag{14}$$

5.2. Diapycnal Diffusivity Coefficient

[45] The estimated K_ρ is temporally averaged over the 4th period. Figure 13a shows the distribution in the vertical cross section of the northeastern island chain, where significant mixing corresponding to values of $K_\rho > 50$ $cm^2\ s^{-1}$ can be seen over a relatively wide area. The maximum value exceeds 1000 $cm^2\ s^{-1}$ over shallow sills. The distribution pattern and magnitude are similar to those of the vertically 2-D case (NA00b) and are in agreement with the results of section 3. Therefore significant diapycnal mixing in this region is attributed to unsteady lee waves. On the contrary, Figure 13b shows the K_ρ map across the deep Bussol' Strait where wave energy generation is much weaker than in the above region. On this map, σ_θ is used as a vertical axis to identify the density layers of active diapycnal mixing. It is apparent that considerable mixing ($K_\rho > 10$ $cm^2\ s^{-1}$) takes place as expected from the results of the energy analysis. This is consistent with the recently observed distributions of carbon isotopes [*Aramaki et al.*, 2001] as well as temperature and salinity [*Kawasaki and Kono*, 1994]. As discussed earlier, this arises from the along-isobath transport of significant wave energy from adjacent shallow sills. It should be noted that the density layer of the neighboring OSMW and NPIW core ($\sim$26.8 σ_θ) is subject to this mixing. Therefore the outflowing Okhotsk Sea water is expected to be modified by tidal mixing to an extent determined by the travel time of passage through the Strait.

[46] The above features relating to the intensity of diapycnal mixing are expected to be general in the Kuril Island Chain. This can be seen in Figure 14, where areas of significant diapycnal mixing at each isopycnal layer in the whole model domain are represented. The figure confirms that intense diapycnal mixing distributes in shallow straits, around islands, and over the bank where tidal flow is swift.

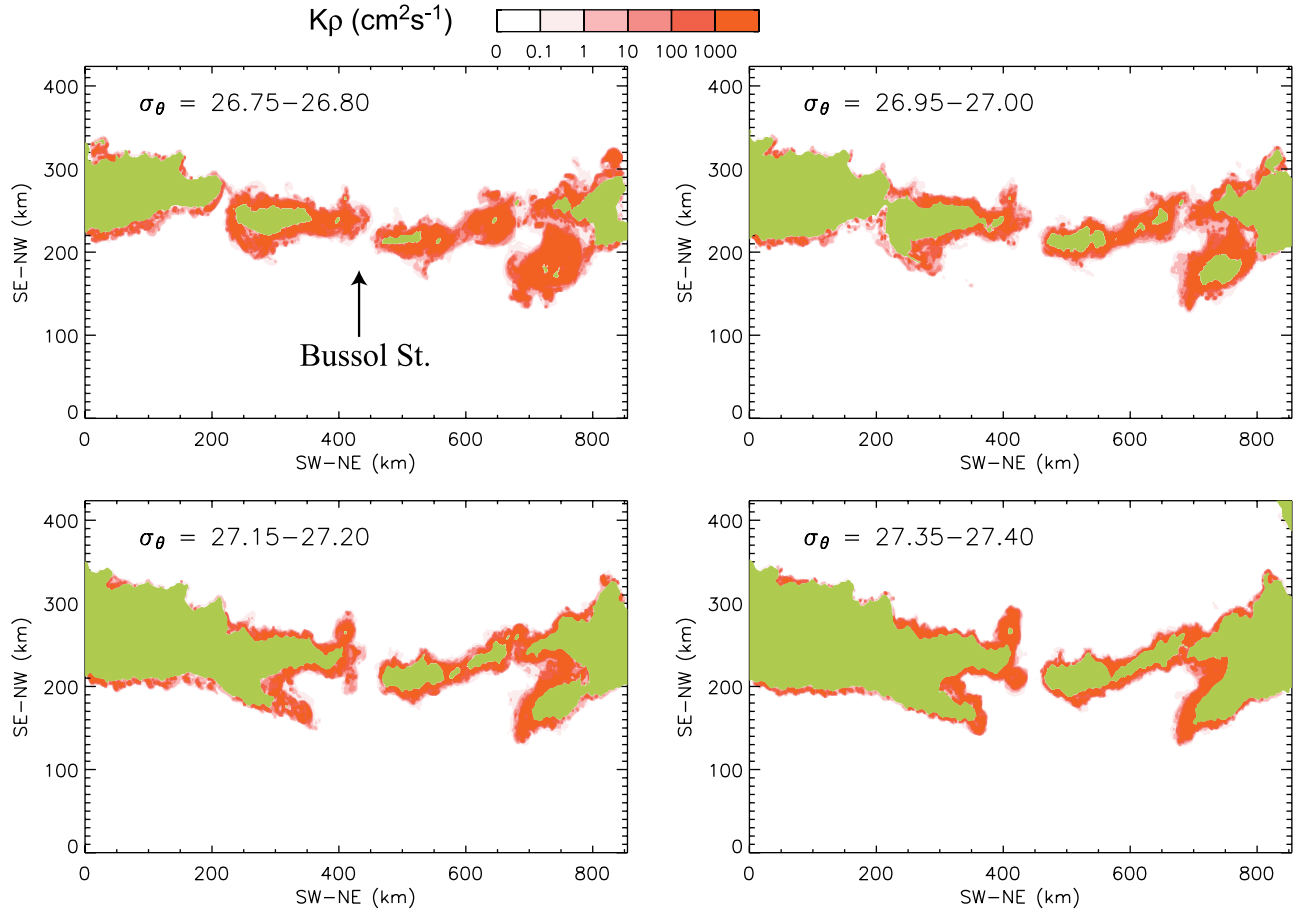

Figure 14. Same as Figure 13b, but for horizontal distribution in four isopycnal layers. Green areas denote land grid points at the corresponding density range.

Hence energetic unsteady lee waves are generated in these regions, whereas the mixing weakens with depth except near the bottom. In addition, K_ρ values averaged at each potential density for water columns of the same water depth in the whole model domain are presented in Figure 13c. These figures are consistent with the high oxygen anomaly in the Kuril Straits observed from the surface to around 2200 m, which is a signature of locally enhanced ventilation [*Yasuoka*, 1968; *Talley*, 1991; *Freeland et al.*, 1998]. Observed chlorofluorocarbons (CFCs) concentrations also indicate the importance of diapycnal mixing in forming the Okhotsk Sea water below 27.2 σ_θ [*Wong et al.*, 1998]. Thus, diapycnal mixing induced by unsteady lee waves and TTWs is the most likely cause of the observed intense vertical mixing at the Kurils, and the estimated values for each isopycnal layer will provide information on how much the vertical density distributions of the water masses are modified in and around the Kuril Straits. For comparison, the K_ρ values averaged horizontally at each depth for water columns of the same water depth in the whole model domain are presented in Figure 13d.

6. Eddy Transport of Transformed Water to the Offshore Region

[47] As mentioned in section 3.1, the pinched-off eddies moving away from tidal fronts have the ability to transport the transformed water from the straits to offshore regions. This spreads the effect of tidal mixing around the islands to the deep basins. In this section, such offshore transport is estimated to assess the impact of tide-induced water modification in and around the straits on the Okhotsk Sea and the North Pacific.

6.1. Eddy-Induced Transport of Mixed Water

[48] To quantify the offshore transport of mixed water around the straits (defined here as transport reaching deep offshore regions), we use PPV to differentiate the mixed water from the surroundings and calculate its volume in deep regions, defined here as >3000 m, because the deepest strait of the Kuril Chain is ~2200 m while the adjacent Kuril Basin is around 3200 m deep and because the estimated diapycnal mixing is rather small in regions deeper than 3000 m except near the bottom (Figure 13). The region where $y > 330$ km is also regarded as the deep region to include the fringe of the Kuril Basin (except for the part near the Kuril Straits), where the mixing is weak but the depth <3000 m. The mixed water is identified as having a PPV value either 20% lower or higher than the ambient average, approximated here as the isopycnal average in a region of almost no PPV anomaly (x = 50 km to 200 km, y = 30 km to 150 km). Following on from these definitions, the volume increase of the mixed water in the deep regions is calculated in order to indicate the offshore transport of the

mixed water, assuming that diapycnal mixing is not effective in the deep regions. Our estimate does not fully remove the influence of horizontal diffusion that is inevitably involved in a numerical model. Note that increase or decrease of the above threshold values of PPV by 5% does not make a qualitative difference.

[49] Figure 15 shows the calculated volumes for each isopycnal layer at five-period intervals. The major offshore transport of low PPV water to the deep regions is conducted through layers lighter than 26.65 σ_θ (Figure 15a). At greater depth, an alternating pattern appears. This shows as a peak of high PPV water around 26.65 σ_θ (Figure 15b), a significant amount of low PPV water around 26.8 σ_θ, and high PPV water in the deep layer. Each peak has its counterpart in shallow regions (Figures 15c and 15d), indicating that their formation regions lie in the Kuril Straits (the shallow region is defined here as a region that is neither the deep region nor the sponge zone). This is not the case for the deepest of the high-PPV anomalies that is produced locally (and is excluded in the following estimates).

[50] Each pair of low and high peaks is preceded by the formation of a low PPV peak. The reason for this is as follows. Intense diapycnal mixing over shallow sill tops (~200 m) produces vertically uniform (thus low PPV) water in the upper layer. As this mixing evolves, high PPV water is formed beneath it and the density of the peak moves to heavier water. The former (latter) corresponds to the first peak of low (high) PPV water. At mid-depths (say 500 m to 1500 m), a similar process occurs associated with considerable diapycnal mixing generated around sill tops of moderate depth and over sill slopes, thereby producing a second peak of low PPV water in the intermediate layer and a second high PPV peak below. Note that water modification is still in effect after 25 periods since the diffusion timescale is longer than in shallower layers because of weaker diapycnal mixing. In addition, the above pattern also depends somewhat on the vertical profile of PPV initially set in this experiment. In this case, the lightest and largest peak of high PPV is enhanced by the presence of the low PPV OSMW.

[51] The total offshore volume flux of low and high PPV waters during 25 periods reaches 5.7 Sv and 8.7 Sv, respectively, on average, of which 2.6 Sv and 3.9 Sv enter the open Pacific. These offshore transports are attributed mainly to eddies arising and moving away from tidal fronts (at least in this model) since the net offshore transports by tidally induced residual flow are about 2 Sv for the Okhotsk Sea and almost nothing for the open North Pacific, which are similar to those in the barotropic case (Figure 4). Figure 15 suggested that the volume increment to the mixed water in the offshore regions is roughly constant around 25 periods because the eddy transport is still in effect. This indicates that the offshore transport is roughly in a steady state and hence that our estimate is meaningful.

[52] Diapycnal mixing within the vicinity of the Kuril Islands therefore has a greater impact than previously thought on the Okhotsk Sea and the North Pacific as a result of both modification of in/outflowing water properties and offshore transport of the modified water due to eddies. This is consistent with a recent analysis of observed oxygen

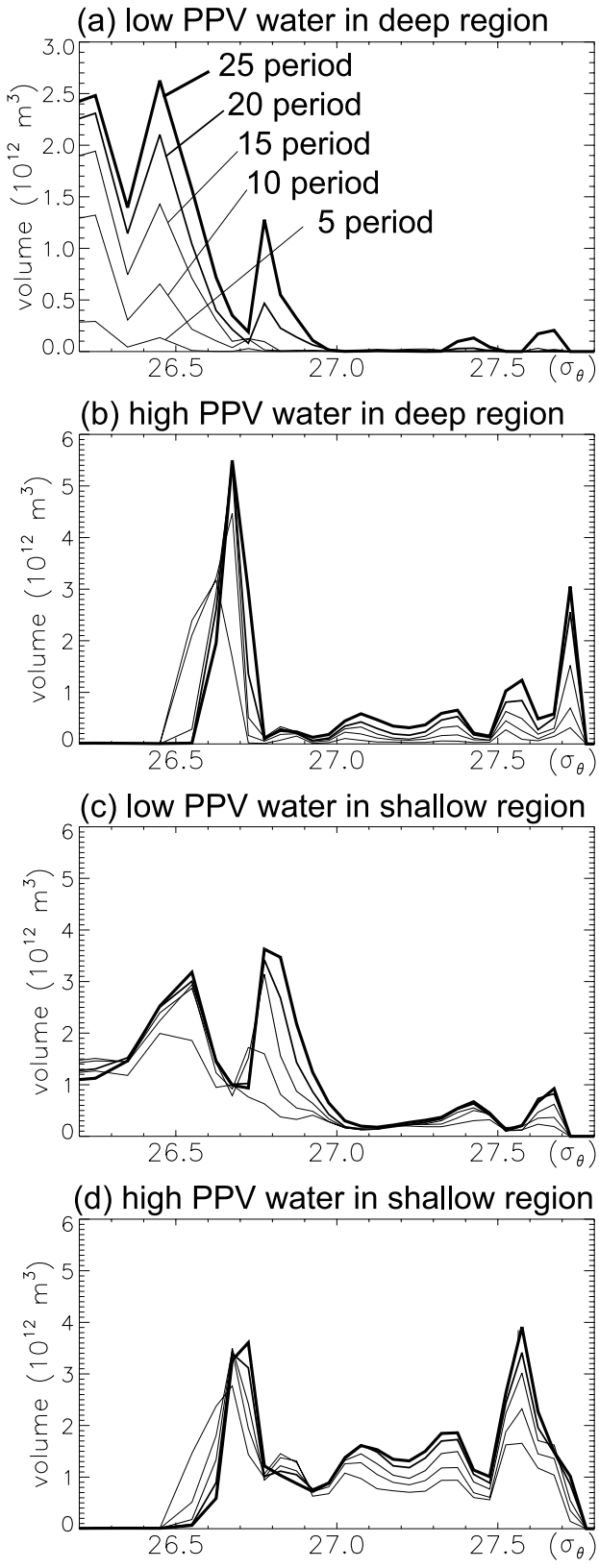

Figure 15. Evolution of anomalous PPV water volume in isopycnal layers. (a) Low and (b) high PPV waters in the offshore area, and (c) low and (d) high PPV waters in the shallow region. Thicker lines indicate later time as indicated in Figure 15a.

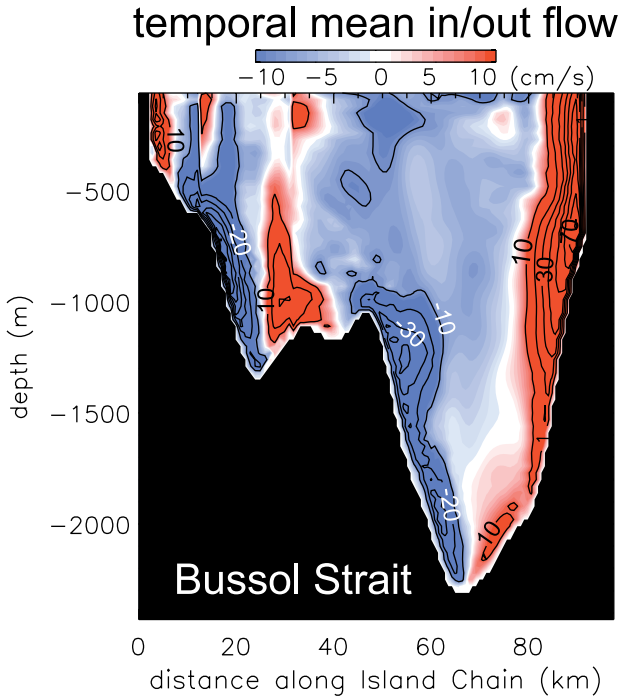

Figure 16. Temporally averaged inflow (red) and outflow (blue) in the Bussol' Strait in the fourth period. Inflow denotes to the Okhotsk Sea from the North Pacific. Contour interval is 10 cm s^{-1}.

isotope distributions that suggests that vertical mixing is more important than the role of sea ice in the formation of the intermediate water of the Okhotsk Sea [*Yamamoto et al.*, 2002].

6.2. PPV and Salinity Transport by Eddies

[53] In association with the eddy-driven transport, water bodies exhibiting locally anomalous properties are conveyed steadily offshore. Here we assess the impact on offshore deep regions focusing on the change in PPV and sea surface salinity. On the basis of the previous section, PPV values of the eddies differ on average by 30% to 40% from the background values. Similarly, the salinity of the eddies differs; for example, the model sea surface salinity of low PPV water is 0.1 psu larger on average than the background value. This induces an increase in potential density by 0.08 σ_θ in offshore regions. (Note that these differences are still increasing after 25 periods.) *Reid* [1973] and *Gladyshev* [1995] reported that high sea-surface-salinity anomalies of 0.1 $\sim$ 0.3 psu greater than the surroundings exist in the Kuril Straits. This implies that tidal mixing in the Kuril Straits induces a significant upward salt flux into the surface layer, which can be subsequently transported to the interior regions of the Okhotsk Sea and the North Pacific. In addition, the PPV flux will affect the circulation in the interior region according to the ventilated thermocline theory. With a saline flux into the surface layer, cooling in winter will produce heavier water and thus enhance subduction.

[54] The above estimation of PPV and salinity fluxes could somewhat change if the initial stratification is altered from that exhibited by the Kuril Basin water to that of the East Kamchatka Current Water. Nevertheless, the close similarities to the observations suggest that our results will not be changed qualitatively.

7. Water Exchange Between the Okhotsk Sea and the North Pacific

[55] To examine the relative importance of the eddy-driven transport, in this section we compare it with a variety of estimates for water exchange through the Kuril Straits.

7.1. Water Exchange by the K_1 Tide

[56] Figure 16 shows a map of the time-averaged current in the vertical cross section of the Bussol' Strait in the fourth period. In general, the mean current flows along the slope with the shallower side on the right and is characterized by a horizontally alternating structure favorable for enhancing the net water exchange as in the barotropic case. In the vertical profile, considerable shear exists. In particular, the current is intensified near the bottom to a significant flow speed of 20 cm s^{-1} or more. These features are qualitatively similar to the findings of the very recent LADCP measurement program [*Katsumata et al.*, 2004], which resolved the complicated current structure in the strait. Moreover, the observed mean flow is stronger near the peak of the fortnight spring tide compared with that of neap tide. These results suggest that the tide is its major forcing.

[57] The time-averaged water exchange through the Kuril Straits in the whole model domain is shown in Figure 17.

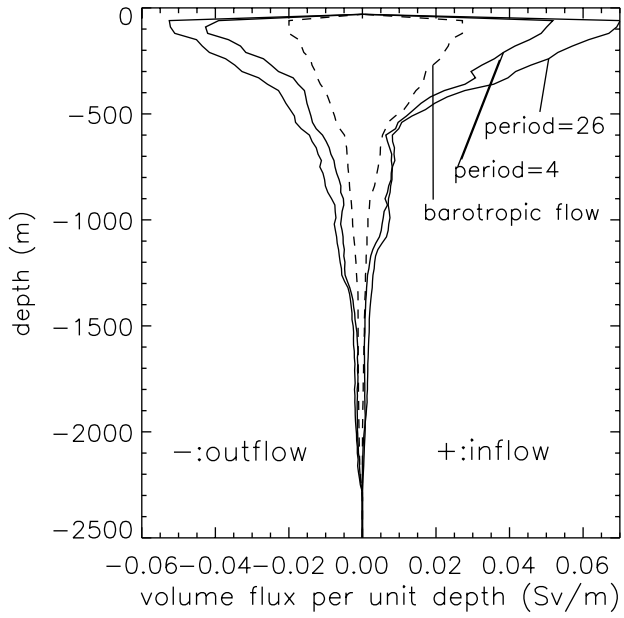

Figure 17. Water exchange through the straits obtained by temporally averaging currents, shown in terms of volume flux per unit depth (Sv/m). Thick and thin lines are those of periods 4 and 26, respectively, and dashed lines are those corresponding to the barotropic flow. The values are integrated in the whole straits in the model, though the northernmost and southernmost parts of the straits are not included. Note that these straits are very shallow (less than 100 m) so that the transport will be as small as in the barotropic case considered by *Nakamura et al.* [2000a].

The total amount of exchanged water reaches 26 Sv in the 26th period, with roughly half passing through the wide and deep Bussol' Strait. This represents a marked increase over that in the barotropic case of NA00a and is mainly due to intensification of the mean flow by the effect of baroclinic waves, as the ''extended'' tidal rectification mechanism suggests [NA00a]. The effect associated with the tidal fronts make an additional contribution in the 26th period. (The increase in the barotropic component from NA00a's estimate is due to the finer grid resolution used here.)

7.2. Comparison With Other Estimates and the Roles of Tide- and Eddy-Induced Transports

[58] There are three observational estimates of outflow to the North Pacific using direct current measurements. From the intensive LADCP measurements mentioned above, *Katsumata et al.* [2004] have estimated an outflow through the Bussol' Strait to be 8.2 $\sim$ 8.8 Sv. Note that horizontal integration was applied to their estimate of these values, and thus the outflow volume would be much larger when taking the bi-directional flow structure into consideration. The outflow for the full island chain was estimated to be 16.7 Sv by *Kurashina et al.* [1967], who combined a variety of ''two current meter,'' GEK, and geostrophic measurements. This value could be also an underestimate since their estimate for the Bussol' Strait is only 4.8 Sv, even smaller than the estimate by *Katsumata et al.* [2004]. An outflow through the Kruzenshterna Strait was estimated to be small (1.6 Sv) [*Katsumata et al.*, 2001].

[59] In contrast, observational estimates based on tracer budgets are much smaller than those based on current measurements. *Wong et al.* [1998] gave an estimate of 2.7 Sv for the density range of 26.6 to 27.4 σ_θ (roughly corresponding to 100–1100 m depth) from θ, S, and CFC budgets in the Okhotsk Sea. By estimation of the mixing ratio between the Okhotsk Sea and the East Kamchatka Current water in the Oyashio Current from θ-S analysis, *Yasuda* [1997] and *Yasuda et al.* [2002] calculated the outflow to be 2 $\sim$ 5 Sv for a 26.6 to 27.2 σ_θ density range (100–900 m depth) and 4.2 Sv for a 26.6–27.5 σ_θ density range (100–1300 m depth), respectively. Even taking into account the facts that these estimates do not include the contribution of surface and deep layers and that estimates based on tracer budgets are sensitive to the assumptions used [*Kobayashi*, 2000], the difference from those based on current measurements nevertheless seems significant.

[60] On the other hand, the present estimate of the tide-induced water exchange via the Kuril Straits is closer to the estimates based on direct current measurements. For example, our simulation experiment forced by the K_1 tide alone explains at least a half of the horizontally integrated outflow volume from the Bussol' Strait reported by *Katsumata et al.* [2004]. This is confirmed by the fact that the corresponding area integration of outflow using our simulation result yields the amount of 4.4 Sv. As for the offshore transport by eddies, the estimated result in section 6.1 is similar to those derived from tracer budgets. Thus, our estimates of the tide- and eddy-induced transports have a gap that is similar to the significant difference in water exchange through the straits described above.

[61] The above comparisons of the outflow evaluations suggest that the gap in the observational estimates has a physical reasoning. Considering the fact that the tide-induced residual flow circulates along isobaths and that most of it is therefore trapped around the islands, the gap is likely to be explained by the joint action of tide-induced residual transport dominating in the vicinity of islands and the offshore eddy-driven transport as follows. While a large amount of water passing through the straits by tide-induced residual current remains in the vicinity of the islands for a while, a fraction of the exchanged water of modified water properties is subsequently transported to the offshore regions by eddies generated from tidal fronts. The direct measurements in the straits observe the first process while the budget calculations correspond to the second.

[62] There are other processes that should be included in the above discussion. First of all, the effects of large-scale wind-driven and thermohaline circulations should be considered. In fact, the presence of significant seasonal and/or interannual variation in transport through the straits is reported [*Kawasaki and Kono*, 1992; *Yasuda et al.*, 2000]. This issue has not been well described and is currently under investigation by several researchers. We note that there are spring-neap cycles of a semi-annual period such as those generated by the K_1 and P_1 tides. Inclusion of these effects are necessary for a more accurate estimates of transport. The variation in the depth of straits also results in a net outflow of 1 Sv by tide-induced mean flow from the deepest Bussol' Strait. This is not counted in the ''offshore transport'' in section 6.1 since it flows over a shelf break that is shallower than 3000 m, as in the barotropic case, though it is confined to the intermediate layers located roughly from 500 m ($\sim$27.0 σ_θ) to 1500 m ($\sim$27.5 σ_θ). Eddies also arise from other mechanisms, such as those originating from the Kuroshio Extension. In addition, there is the difficult matter of the relation between Lagrangian and Eulerian transports. For example, tidally induced residual transport could make a significant contribution when interacting with eddies. These problems should be further investigated in the future. Nevertheless, good similarities with observations have been found in our modeling results, in particular regarding the presence of mixed water produced by strong tidal currents in the straits and the presence of many eddies [*Talley and Nagata*, 1995; *Yasuda et al.*, 2000]. Moreover, long-term observations by *Kono and Kawasaki* [1997] pointed to the fact that pure Okhotsk Sea water hardly reaches offshore of Hokkaido (just downstream of the Kuril Island Chain) and that the East Kamchatka Current water has already been modified before the confluence with Okhotsk Sea water from the Bussol' Strait. Our model result is able to explain these observational facts. As such, the concept that water exchange through the straits and offshore transport is dominated by a number of separate physical processes will be useful in better understanding the relation between the Okhotsk Sea and the North Pacific as well as the impact of tidal processes in the Kuril Straits.

[63] We suspect that both eddy genesis from tidal fronts and tidally induced residual flow circulating around an island also work as the major causes of isopycnal mixing for the Okhotsk Sea water and the East Kamchatka Current

water. These problems are beyond the present model configuration and are left for future work.

8. Summary and Discussion

[64] An experiment using a 3-D nonhydrostatic model was conducted in order to investigate water transformation and transport processes associated with the K_1 tide around the Kuril Straits. These processes are considered to be central in our understanding of the linkage between the Okhotsk Sea and the North Pacific via the Kuril Straits. The results obtained are as follows.

[65] As in the vertically 2-D case, large-amplitude unsteady lee waves are generated around a sill top and propagate away as the flow reverses. The generation regions of intense internal waves with a maximum elevation higher than 200 m correspond to areas where the energy conversion from the barotropic tidal flow to potential energy is large. Such zones have been identified as (1) the bank on the Pacific side of the northeastern Kurils, (2) the Urup Strait, and (3) sills in the northeast of the study area. As a result, significant wave breaking occurs from the sea surface to about the 27.6 σ_θ density layer. Though firm experimental evidence to support these prediction of wave generation is required, some internal-wave-like signatures observed in LANDSAT-4 TM visible-band imagery provide encouragement that our simulated results are indicative of the real situation. Over the sill slope, subinertial K_1 internal tides are generated as topographically trapped waves and propagate clockwise along isobaths. The propagation of these two kinds of waves is accompanied by energy flux from the regions of strong tidal flow to greater depths.

[66] The wave generation and energy flow eventually cause intense diapycnal mixing over the shallow sills and bank and near the bottom leading to the maximum diapycnal diffusivity of over 1000 $cm^2\ s^{-1}$. These same locations are also the generation regions of unsteady lee waves. Interestingly, considerable mixing takes place ($10 \sim 50\ cm^2\ s^{-1}$) even in the deep Bussol' Strait, which is thought to be the main exit of the Okhotsk Sea water. This is mainly due to energy supply carried by the two types of wave from the adjacent Urup and Simusir Straits where energetic wave generation occurs.

[67] The intense mixing transforms water properties in and around the straits and thereby produces an upper layer of well-mixed low potential vorticity (PV) water with a layer of high PV water below. Accordingly, PV fronts are formed around the islands, and these can sustain instabilities and eventually lead to the formation and release of eddies with low core PV values. Though a robust comparison with satellite imagery awaits a more detailed future study, the calculated distribution of sea surface temperature nevertheless bears an encouraging resemblance to an advanced very high resolution radiometer (AVHRR) sea surface temperature image gathered on 21 September 1994. The similarities identified here imply that the tidal mixing process alone is responsible for frontogenesis and associated eddy formation in the vicinity of the Kuril Islands.

[68] The offshore volume transport away from islands by these eddies reaches 14.4 Sv on average, with some 6.5 Sv being carried to the open North Pacific. This amount is similar to the previous outflow estimates based on tracer budgets. On the other hand, water passing through the straits due to tidal residual flow reaches 26 Sv. Though this value is huge, both the pattern and the amount of exchanged water are in good agreement with the results of direct current measurements in the straits. In particular, the resemblance in the Bussol' Strait with the recent observation by the Hokkaido University group [*Katsumata et al.*, 2004] is striking. These comparisons strongly suggest that our model results are not unrealistic, and we infer that (1) water exchange through the Kuril Straits is mainly caused by tides but (2) most of it is trapped and circulates around the islands as a tidally induced residual flow, and (3) the eddies arising from tidal fronts are mainly responsible for the offshore transport of exchanged water subject to transformation in the straits. Direct measurements in the straits observe the first two processes while the tracer budget analysis corresponds to the last.

[69] Significant offshore eddy transport away from the island region further implies that the effect of diapycnal mixing, which dominates at the Kurils, spreads to the Okhotsk Sea and the North Pacific. In fact, the offshore eddy transport of the transformed water in the straits supplies significant PV and salinity fluxes to both the Okhotsk Sea and the North Pacific. The PV values of such eddies differ by 30–40% from the ambient water. The sea surface salinity is 0.1 psu higher than the ambient water, and this difference leads to a density increase of 0.08 σ_θ in the offshore regions. Such fluxes will affect water masses and circulations in the two basins. Our results imply that the joint effect of tidally induced transport and transformation dominating in the straits and subsequent offshore eddy transport are essential aspects of the link between the Okhotsk Sea and the North Pacific Ocean.

[70] As mentioned in section 2.2, this study adopts a "surface lead assumption"; that is, a barotropic tide used in our 3-D model experiment is calculated separately from a barotropic tide model and is given as the main forcing for the baroclinic process. This assumption is accompanied by the following three approximations.

[71] First of these is a hydrostatic approximation for the barotropic tide model. This is considered to be permissible because the barotropic waves we concern have elevation amplitude of at most 2 m and wavelength of tens to thousands of kilometers (NA00a).

[72] Second, sea surface is approximated to be rigid for a baroclinic component. This leads to the neglect of both nonlinear interaction between barotropic and baroclinic components through displacement of the sea surface and the difference in internal wave reflection at the surface from the free surface case. Errors arising from the neglect of the nonlinear interaction through surface displacements are considered not to be significant since the phase speeds of barotropic tides and baroclinic motions are generally much different from each other so that resonant interaction may hardly occur. Regarding the difference in the reflection at the surface, the linear internal wave theory shows that the difference in reflection between the rigid and free surface cases is indistinguishable (precisely, within an error of the Boussinesq approximation) under the conditions that the surface displacement due to an internal wave is sufficiently smaller than the vertical scale of the wave, and that the wave frequency squared is sufficiently smaller than the

buoyancy frequency squared [e.g., *LeBlond and Mysak*, 1978]. In our numerical experiment (section 3.2), though there are waves of large amplitude ($\sim$100 m), their surface displacement is at most $\sim$0.1 m, much smaller than their vertical wavelength (O(100 m)). Also, the squared frequencies of unsteady lee waves are much smaller than the buoyancy frequency squared (say, $\sim(5/30)^2 = 1/36$). In fact, many previous studies such as that of *Hibiya* [1988] and *Lamb* [1994] successfully reproduced internal wave processes using the rigid lid approximation. Thus the result obtained in this study is considered to be reasonable at least qualitatively.

[73] Last, the energy dissipation of a barotropic tide over a topographic feature is strengthened primarily through the conversion to baroclinic potential energy. The baroclinic motions induced by this energy supply then produce the Reynolds stress, which causes the secondary conversion of kinetic energy between the barotropic and baroclinic motions, and could further strengthen the damping of the barotropic tides.

[74] In the present numerical approach, however, such dissipation of a barotropic tide is included as a result of using the bottom friction and horizontal eddy viscosity in the barotropic tide model. Though these are crude parameterizations, a barotropic tide is well reproduced in many studies by using the above parameterizations, as shown by *Le Provost et al.* [1994] for the global ocean and *Kowalik and Polyakov* [1998] and NA00a for the Okhotsk Sea and the Kuril Straits. In addition, the surface elevation and flow speed of the barotropic tide calculated in this study agree by and large with those of observations as discussed in section 2.4.

[75] The secondary energy conversion through the Reynolds stress can cause some feedback to the barotropic tide, but it is neglected for dynamical consistency with the surface lead assumption in this study. Since this could modify the calculated field, we estimated the energy conversion through the Reynolds stress (using the result calculated without the Reynolds stress term). This term is significant over relatively shallow sills, so that the horizontal distribution of the energy input from the Reynolds stress is basically similar to that of the potential energy supply from the barotropic tide (section 4). The ratio of these two energy source terms averaged in the model domain is 0.46 and 0.48 in the fourth and 26th periods, respectively. Suppose that the fraction of the energy used for local mixing is nearly the same as in the case without the Reynolds stress, the above ratio means that the values of diapycnal mixing coefficient shown in section 5 would increase by 1.5 times. Therefore the Reynolds stress term should be taken into account in order to make more precise estimates in the future. Nevertheless, the distribution of diapycnal mixing would not change qualitatively. Besides, as the Reynolds stress will enhance the energy input to the baroclinic component, the tidally induced processes could be of greater importance than in this study.

[76] From the above discussion, the use of the surface lead assumption and the associated approximations will not change the conclusions obtained in this study qualitatively. This is also supported by the encouraging resemblances between the model results and observations mentioned earlier.

[77] The present study is a first step toward clarifying the baroclinic process in the Kuril Straits and its influence on the North Pacific and the Okhotsk Sea circulation. Our work is a modeling study of one possible process associated with the predominant K_1 tide. In fact, the process is isolated by idealizing the background states. Thus our process study should be complemented by observational studies and comprehensive models with more realistic forcing and capable of investigating the roles of wind-driven and thermohaline circulations on the transport and transformation processes in and around the Kuril Straits. Thus future modifications to our numerical model should provide more realistic simulations. The generation of intense unsteady lee waves implies that an internal wave drag is effective not only for superinertial tides, as considered by *Jayne and Laurent* [2001], but also for subinertial tides as an energy dissipation mechanism in deep regions. This is an interesting issue, but its overall relevance to the energy budget of barotropic tides should be evaluated on the basis of future observations. Nevertheless, the many similarities to observations described above strongly support our qualitative conclusions and confirm/underline the importance of the processes considered here.

Appendix A: Pressure Equation

[78] In general, the pressure field of nonhydrostatic equations for an incompressible fluid can be found by solving a Poisson equation, which is derived from the divergence of the momentum equation. For computational efficiency, we use an iterative method for the Poisson equation. To enhance the convergence of the inversion, the pressure is separated into hydrostatic and nonhydrostatic parts, following *Marshall et al.* [1997b]. The hydrostatic part (p_{HY}) is defined so as to satisfy the hydrostatic balance,

$$\frac{\partial p_{HY}}{\partial z} = -\frac{\rho}{\rho_0} g. \tag{A1}$$

The nonhydrostatic part (p_{NH}) is obtained from the following Poisson equation:

$$\frac{1}{\rho_0}\nabla^2 p_{NH} = \boldsymbol{\nabla}\cdot\left(-\frac{\partial \mathbf{u}}{\partial t} - (\mathbf{u}+\mathbf{U})\cdot\nabla\mathbf{u} - f\mathbf{k}\times\mathbf{u} + \nu_H\nabla_H^2\mathbf{u} + \nu_Z\frac{\partial^2\mathbf{u}}{\partial z^2}\right), \tag{A2}$$

with a homogeneous Neuman boundary condition ($\mathbf{n}\cdot\nabla p_{NH} = 0$), where $\mathbf{n}$ is a unit vector normal to a boundary. More detailed discussions are given by *Harlow and Welch* [1965], *Williams* [1969], and *Marshall et al.* [1997b].

Appendix B: Energy Equation

[79] The energy equation used in section 4 is derived in the following way. First, a dot product of $\rho_0\mathbf{u}$ with the momentum equation (2) yields an equation for the internal mode kinetic energy (*KE*),

$$\left[\frac{\partial}{\partial t} + (\mathbf{u}+\mathbf{U})\cdot\nabla\right]KE + \nabla\cdot(\mathbf{u}p) = -\rho' g w + D_{\mathbf{u}}, \tag{B1}$$

where the term $(-\rho' g w)$ represents the energy conversion from potential energy (PE) to *KE*, and $D_{\mathbf{u}}$ is the dissipation

term. In the derivation of the conversion term, the density variation is expressed as the sum of a horizontal average $\overline{()}^{xy}$ and its deviation $()'$,

$$\rho_{total} = \rho_0 + \overline{\rho}^{xy}(z,t) + \rho'(x,y,z,t). \tag{B2}$$

The dynamically irrelevant part, $-\overline{\rho}^{xy}gw$, is subtracted. This latter term gives rise to the variation of PE due to the interaction with the outside of the model domain through an open boundary, but the restoring condition used here works to keep the domain almost closed, and thus it is negligible in this case.

[80] Second, in order to easily estimate a dynamically relevant part of PE, we define *APE* as in equation (10) following *Gill* [1982]. Since this definition invokes an approximation,

$$\rho' \approx -\frac{d\overline{\rho}^{xy}}{dz}\eta, \tag{B3}$$

for an isopycnal elevation, η, the density used for the definition should be conserved at least approximately. Thus we use the potential density for *APE*. An equation of potential density is

$$\frac{\partial \rho|_{p=0}}{\partial t} + \nabla\cdot(\mathbf{u}+\mathbf{U})\rho|_{p=0} = D'_\rho. \tag{B4}$$

Here the term D'_ρ represents the diffusion of salinity and potential temperature and includes the cabbeling effect though, in this case, the maximum variation in potential temperature is about 1°C except for the surface layer so that the cabbeling effect is very small. The product of equation (B4) and $g\eta$ yields an equation for *APE*,

$$\left[\frac{\partial}{\partial t} + (\mathbf{u}+\mathbf{U})\cdot\boldsymbol{\nabla}\right](APE) + \frac{APE}{\overline{N^2}^{xy}_{p=0}}\left[\frac{\partial}{\partial t} + (w+W)\frac{\partial}{\partial z}\right]\overline{N^2}^{xy}_{p=0} + \frac{\rho'|_{p=0}g}{\rho_0}\frac{\left(\partial\overline{\rho}^{xy}_{p=0}/\partial t\right)}{\left(\partial\overline{\rho}^{xy}_{p=0}/\partial z\right)} = \rho'|_{p=0}g(w+W) + D_\rho, \tag{B5}$$

where $N^2|_{p=0}$ is a squared buoyancy frequency calculated using potential density and D_ρ is the diffusion term.

[81] The second and third terms on the left-hand side of equation (B5) are the correction terms to the first term arising from the approximation (B3). To simplify further, we replace a horizontal average of potential density $\overline{\rho}^{xy}_{p=0}(z,\ t)$ with its temporal average over one tidal cycle $\overline{\rho}^{xyt}_{p=0}(z)$. Then the correction terms become

$$\frac{APE(w+W)}{\overline{N^2}^{xyt}_{p=0}}\frac{\partial}{\partial z}\overline{N^2}^{xyt}_{p=0}. \tag{B6}$$

[82] Finally, using equation (B6), the sum of equations (B1) and (B5) gives the energy equation (7),

$$\frac{\partial E}{\partial t} + \boldsymbol{\nabla}\cdot[(\mathbf{u}+\mathbf{U})E + \mathbf{u}p] + \frac{APE(w+W)}{\overline{N^2}^{xyt}_{p=0}}\frac{\partial}{\partial z}\overline{N^2}^{xyt}_{p=0} = -\left(\rho' - \rho'|_{p=0}\right)gw + \rho'|_{p=0}gW + D_{\mathbf{u}} + D_\rho. \tag{B7}$$

In the above, the term $\rho'|_{p=0}gW$ represents an energy supply from the barotropic tidal flow (kinetic energy) to *APE*, which is almost all of the energy source of the model (the sponge zone mainly acts as an energy sink).

[83] Another correction term arises from the use of potential density in *APE*. The terms $\rho'|_{p=0}gw$ and $-\rho'gw$ represent energy conversions from *KE* to *APE* and PE to *KE*, respectively. The sum of these two would vanish if we used an general expression of *PE* instead of the *APE*, and can be regarded as a correction to the variation of *APE* (due to the compressibility). Although use of PE allows us to circumvent these two correction terms, it makes the definition of energy flux vectors due to advection difficult. We thus use the *APE* since we are interested in energy transport.

[84] We choose the averaged density in equation (B3) in order to avoid a singularity and to enable a robust calculation of *APE* even in the presence of density inversions. However, it should be noted that the use of $\partial\rho/\partial z$ instead of the average reduces the equation (B6) part of the correction term when there are no density inversions. The reason for this is that when the averaged buoyancy frequency varies in the vertical direction, the former method leads to an overestimate of η for a vertical displacement extending to the layer with greater buoyancy frequency and vice versa.

[85] **Acknowledgments.** We greatly appreciate the kind offer of use of the numerical model from K. Tanaka and K. Akitomo. We also wish to acknowledge J. P. Matthews for his critical reading and for the kind offer of LANDSAT-TM imagery, and S. Saitoh (Hokkaido University, Japan) for the kind offer of NOAA 12 AVHRR imagery. Thanks are extended to anonymous reviewers for their useful comments and to S. Martin and K. Ohshima, who are the associate editors of the special section, for their comments on the figures. Numerical calculations were done on the VPP800 at the Data Processing Center of Kyoto University. T. A. and T. N. are partly supported by Category 7 of MEXT RR2002 Project for Sustainable Coexistence of Human, Nature and the Earth. T. N. is also supported by a JSPS Research Fellowship for Young Scientists.

References

Alpers, W. (1985), Theory of radar imaging of internal waves, *Nature*, *314*, 245–247.

Apel, J. R., H. M. Byrne, J. R. Proni, and R. L. Charnell (1975), Observation of oceanic internal and surface waves from the Earth Resources Technology Satellite, *J. Geophys. Res.*, *80*, 865–881.

Aramaki, T., S. Watanabe, T. Kuji, and M. Wakatsuchi (2001), The Okhotsk-Pacific seawater exchange in the viewpoint of vertical profiles of radiocarbon around the Bussol' Strait, *Geophys. Res. Lett.*, *28*, 3971–3974.

Awaji, T., N. Imasato, and K. Kunishi (1980), Tidal exchange through a strait: A numerical experiment using a simple model basin, *J. Phys. Oceanogr.*, *10*, 1499–1508.

Boss, E., and L. Thompson (1999), Lagrangian and tracer evolution in the vicinity of an unstable jet, *J. Phys. Oceanogr.*, *29*, 288–303.

Chapman, D. C. (1989), Enhanced subinertial diurnal tides over isolated topographic features, *Deep Sea Res.*, *36*, 815–824.

Chen, C., and R. C. Beardsley (1995), A numerical study of stratified tidal rectification over finite-amplitude banks: I. Symmetric banks, *J. Phys. Oceanogr.*, *25*, 2090–2110.

Cummins, P. F., D. Masson, and M. G. G. Foreman (2000), Stratification and mean flow effects on diurnal tidal currents off Vancouver Island, *J. Phys. Oceanogr.*, *30*, 15–30.

Favorite, F., A. J. Dodimead, and K. Nasu (1976), Oceanography of the Subarctic Pacific region: 1960–1971, *Bull Int. N. Pac. Fish. Comm.*, *33*, 187 pp.

Freeland, H. J., A. S. Bychkov, F. Whitney, C. Taylor, C. S. Wong, and G. I. Yurasov (1998), WOCE section P1W in the Sea of Okhotsk: 1. Oceanographic data description, *J. Geophys. Res.*, *103*, 15,613–15,623.

Gill, A. E. (1982), *Atmosphere-Ocean Dynamics*, 662 pp., Academic, San Diego, Calif.

Gladyshev, S. V. (1995), Fronts in the Kuril Island region, *Oceanology, Engl. Transl.*, *34*, 452–459.

Gregg, M. C. (1989), Scaling turbulent dissipation in the thermocline, *J. Geophys. Res.*, *94*, 9686–9698.

Haidvogel, D. B., A. Beckmann, D. C. Chapman, and R. Q. Lin (1993), Numerical simulation of flow around a tall isolated seamount: II. Resonant generation of trapped waves, *J. Phys. Oceanogr.*, *23*, 2373–2391.

Harlow, F. H., and J. E. Welch (1965), Numerical calculation of time-dependent viscous incompressible flow of fluid with a free surface, *Phys. Fluids*, *8*, 2182–2193.

Hibiya, T. (1988), The generation of internal waves by tidal flow over Stellwagen Bank, *J. Geophys. Res.*, *93*, 533–542.

Hsieh, W. W. (1982), On the detection of continental shelf waves, *J. Phys. Oceanogr.*, *12*, 414–427.

Huthnance, J. M. (1973), Tidal current asymmetries over the Norfolk Sandbank, *Estuarine Coastal Mar. Sci.*, *1*, 89–99.

Isoguchi, O., H. Kawamura, and T. Kono (1997), A study on wind-driven circulation in the subarctic North Pacific using TOPEX/Poseidon altimeter data, *J. Geophys. Res.*, *102*, 12,457–12,468.

Jackett, D. R., and T. J. McDougall (1995), Minimal adjustment of hydrographic profiles to achieve static stability, *J. Atmos. Oceanic Technol.*, *12*, 381–389.

Jayne, S. R., and L. C. St. Laurent (2001), Parameterizing tidal dissipation over rough topography, *Geophys. Res. Lett.*, *28*, 811–814.

Katsumata, K., I. Yasuda, and Y. Kawasaki (2001), Direct current measurements at Kruzenshterna Strait in summer, *Geophys. Res. Lett.*, *28*, 319–322.

Katsumata, K., K. I. Ohshima, T. Kono, M. Itoh, I. Yasuda, and M. Wakatsuchi (2004), Water exchange and tidal current through the Bussol' Strait revealed by direct current measurements, *J. Geophys. Res.*, *109*, C09S06, doi:10.1029/2003JC001864, in press.

Kawasaki, Y. (1996), The origin of the North Pacific Intermediate Water—From the observations in the Okhotsk Sea (in Japanese), *Kaiyo Mon.*, *28*, 545–552.

Kawasaki, Y., and T. Kono (1992), Baroclinic water exchange in the Kuril Basin and the northwestern Pacific in summer (in Japanese with English abstract and figure captions), *Sea Sky*, *68*, 41–54.

Kawasaki, Y., and T. Kono (1994), Distribution and transport of subarctic Waters around the middle of Kuril Islands (in Japanese with English abstract and figure captions), *Sea Sky*, *70*, 71–84.

Kitani, K. (1973), An oceanographic study of the Okhotsk Sea—Particularly in regard to cold waters, *Bull. Far Seas Fish. Res. Lab.*, *9*, 45–77.

Kobayashi, T. (2000), Estimation of the freshwater transport and the water exchange through the passages of the Kuril Islands (in Japanese), *Sea Sky*, *76*, 153–160.

Kono, T. (1998), Formation of the salinity minimum in the Mixed Water Region between the Oyashio and Kuroshio Fronts, *Deep Sea Res., Part I*, *45*, 2035–2057.

Kono, T., and Y. Kawasaki (1997), Modification of the western subarctic water by exchange with the Okhotsk Sea, *Deep Sea Res., Part I*, *44*, 689–711.

Kowalik, Z., and I. Polyakov (1998), Tides in the Sea of Okhotsk, *J. Phys. Oceanogr.*, *28*, 1389–1409.

Kowalik, Z., and A. Y. Proshutinsky (1995), Topographic enhancement of tidal motion in the western Barents Sea, *J. Geophys. Res.*, *100*, 2613–2637.

Kurashina, S., K. Nishida, and S. Nakabayashi (1967), On the open water in the southeastern part of the frozen Okhotsk Sea and the currents through the Kuril Islands (in Japanese with English abstract and figure captions), *J. Oceanogr. Soc. Jpn.*, *23*, 57–62.

Lamb, K. G. (1994), Numerical experiments of internal wave generation by strong tidal flow across a finite amplitude bank edge, *J. Geophys. Res.*, *99*, 843–864.

LeBlond, P. H., and L. A. Mysak (1978), *Waves in the Ocean*, 602 pp., Elsevier Sci., New York.

Leonard, B. P. (1979), A stable and accurate convective modelling procedure based on quadratic upstream interpolation, *Comput. Methods Appl. Mech. Eng.*, *19*, 59–98.

Leonov, A. K. (1960), *Regional Oceanography, Part 1*, 766 pp., Gidrometeoizdat, Leningrad, Russia.

Le Provost, C., M. L. Genco, F. H. Lyard, P. Vincent, and P. Canceil (1994), Spectroscopy of the world ocean tides from a finite element hydrodynamic model, *J. Geophys. Res.*, *99*, 24,777–24,797.

Marshall, J., A. Adcroft, C. Hill, L. Perelman, and C. Heisey (1997a), A finite-volume, incompressible Navier Stokes model for studies of the ocean on parallel computers, *J. Geophys. Res.*, *102*, 5753–5766.

Marshall, J., C. Hill, L. Perelman, and A. Adcroft (1997b), Hydrostatic, quasi-hydrostatic, and nonhydrostatic ocean modeling, *J. Geophys. Res.*, *102*, 5733–5752.

Moroshkin, K. V. (1966), Water masses of the Sea of Okhotsk, *Rep. 43*, 98 pp., Joint Publ. Res. Serv., U.S. Dep. of Commer., Washington, D. C.

Nakamura, T., and T. Awaji (2001), A growth mechanism for topographic internal waves generated by an oscillatory flow, *J. Phys. Oceanogr.*, *31*, 2511–2524.

Nakamura, T., T. Awaji, T. Hatayama, K. Akitomo, and T. Takizawa (2000a), Tidal exchange through the Kuril Straits, *J. Phys. Oceanogr.*, *30*, 1622–1644.

Nakamura, T., T. Awaji, T. Hatayama, K. Akitomo, T. Takizawa, T. Kono, Y. Kawasaki, and M. Fukasawa (2000b), The generation of large-amplitude unsteady lee waves by subinertial K_1 tidal flow: A possible vertical mixing mechanism in the Kuril Straits, *J. Phys. Oceanogr.*, *30*, 1601–1621.

Ohshima, K. I., M. Wakatsuchi, Y. Fukamachi, and G. Mizuta (2002), Near-surface circulation and tidal currents of the Okhotsk Sea observed with the satellite-tracked drifters, *J. Geophys. Res.*, *107*(C11), 3195, doi:10.1029/2001JC001005.

Pedlosky, J. (1987), *Geophysical Fluid Dynamics*, 2nd ed., 710 pp., Springer-Verlag, New York.

Pedlosky, J. (1996), *Ocean Circulation Theory*, 453 pp., Springer-Verlag, New York.

Polzin, K., J. M. Toole, and R. W. Schmitt (1995), Finescale parameterizations of turbulent dissipation, *J. Phys. Oceanogr.*, *25*, 306–328.

Qiu, B., N. Imasato, and T. Awaji (1988), Baroclinic instability of buoyancy-driven coastal density currents, *J. Geophys. Res.*, *93*, 5037–5050.

Rabinovich, A. B., and R. E. Thomson (2001), Evidence of diurnal shelf waves in satellite-tracked drifter trajectories off the Kuril Island, *J. Phys. Oceanogr.*, *31*, 2650–2668.

Reid, J. L. (1965), *Intermediate Waters of the Pacific Ocean*, 85 pp., Johns Hopkins Univ. Press, Baltimore, Md.

Reid, J. L. (1973), *North Pacific Ocean Waters in Winter*, 85 pp., Johns Hopkins Univ. Press, Baltimore, Md.

Ridderinkhof, H. (1989), Tidal and residual flows in the Western Dutch Wadden Sea: Vorticity balances, *Neth. J. Sea Res.*, *24*, 9–16.

Robinson, I. S. (1981), Tidal vorticity and residual circulation, *Deep Sea Res., Part A*, *28*, 195–212.

Schwiderski, E. W. (1980), On charting global ocean tides, *Rev. Geophys.*, *18*, 243–268.

Scinocca, J. F., and W. R. Peltier (1994), The instability of Long's stationary solution and the evolution toward severe downslope windstorm flow: I. Nested grid numerical simulations, *J. Atmos. Sci.*, *50*, 2245–2263.

Simpson, J. H., C. M. Allen, and N. C. G. Morris (1978), Fronts on the continental shelf, *J. Geophys. Res.*, *83*, 4607–4614.

Talley, L. D. (1991), An Okhotsk Sea water anomaly: Implications for ventilation in the North Pacific, *Deep Sea Res.*, *38*, s171–190.

Talley, L. D. (1993), Distribution and formation of North Pacific Intermediate Water, *J. Phys. Oceanogr.*, *23*, 517–537.

Talley, L. D., and Y. Nagata (1995), *The Okhotsk Sea and Oyashio region*, *PICES Sci. Rep. 2*, 227 pp., PICES Secr., Sidney, B. C., Can.

Tanaka, K., and K. Akitomo (2001), Baroclinic instability of density current along a sloping bottom and the associated transport process, *J. Geophys. Res.*, *106*, 2621–2638.

Thomson, R. E., P. H. LeBlond, and A. B. Rabinovich (1997), Oceanic odyssey of a satellite-tracked drifter: North Pacific variability delineated by a single drifter trajectory, *J. Oceanogr.*, *53*, 81–87.

Tsunogai, S., T. Ono, and S. Watanabe (1993), Increase in total carbonate in the western North Pacific water and a hypothesis on the missing sink of anthropogenic carbon, *J. Oceanogr.*, *49*, 305–315.

Watanabe, T., and M. Wakatsuchi (1998), Formation of 26.8 σ_θ water in the Kuril Basin of the Sea of Okhotsk as a possible origin of North Pacific Intermediate Water, *J. Geophys. Res.*, *103*, 2849–2865.

Williams, G. P. (1969), Numerical integration of the three-dimensional Navier Stokes equations for incompressible flow, *J. Fluid Mech.*, *37*, 727–750.

Wong, C. S., R. J. Matear, H. J. Freeland, F. A. Whitney, and A. S. Bychkov (1998), WOCE line P1W in the Sea of Okhotsk: 2. CFCs and the formation rate of intermediate water, *J. Geophys. Res.*, *103*, 15,625–15,642.

Wüst, G. (1930), Meridionale Schichtung und Tiefenzirkulation in der Westhalften der drei Ozeane, *Journal Cons. Cons. Int. Explor. Mer*, *5*, 21 pp.

Yamamoto, M., S. Watanabe, S. Tsunogai, and M. Wakatsuchi (2002), Effects of sea ice formation and diapycnal mixing on the Okhotsk Sea Intermediate Water clarified with oxygen isotopes, *Deep Sea Res., Part I*, *49*, 1165–1174.

Yamanaka, Y., and E. Tajika (1996), The role of the vertical fluxes of particulate organic matter and calcite in the oceanic carbon cycle: Studies using biogeochemical general circulation model, *Global Biogeochem. Cycles*, *10*, 361–382.

Yasuda, I. (1997), The origin of the North Pacific Intermediate Water, *J. Geophys. Res.*, *102*, 893–910.

Yasuda, I., K. Okuda, and Y. Shimizu (1996), Distribution and formation of North Pacific Intermediate Water in the Kuroshio-Oyashio interfrontal zone, *J. Phys. Oceanogr.*, *26*, 448–465.

Yasuda, I., et al. (2000), Cold-core anticyclonic eddies south of the Bussol' Strait in the northwestern Subarctic Pacific, *J. Phys. Oceanogr.*, *30*, 1137–1157.

Yasuda, I., S. Kouketsu, K. Katsumata, M. Ohiwa, Y. Kawasaki, and A. Kusaka (2002), Influence of Okhotsk Sea intermediate water on the Oyashio and North Pacific Intermediate Water, *J. Geophys. Res.*, *107*(C12), 3237, doi:10.1029/2001JC001037.

Yasuoka, T. (1968), Hydrography in the Okhotsk Sea-(2), *Oceanogr. Mag.*, *20*, 55–63.

T. Awaji, Department of Geophysics, Graduate School of Science, Kyoto University, Kyoto 606-8502, Japan.

T. Nakamura, Integrated Modeling Program, Frontier Research System for Global Change, Yokohama 236-0001, Japan. (tnakamura@jamstec.go.jp)